STUDIES OF CRYSTAL STRUCTURE USING MULTIPHOTON TRANSITIONS IN GaAs

SARAH M. GOLIN

A thesis submitted to the Department of Physics
in conformity with the requirements for
the degree of Master of Science

University of Ottawa
150 Louis Pasteur, Ottawa, Canada
August 2012

Abstract

We demonstrate experimentally that the multiphoton ionization rate in gallium arsenide depends on the alignment of the laser polarization with respect to the crystal axis. We show real-time modulation of 1900nm laser ionization rate, through viewing transmission, which mimics the symmetry of the semiconductor crystal. We propose that the modulation in the ionization rate arises because the varying reduced effective carrier mass, as predicted by Keldysh theory. We show direct comparison of the experimental transmission modulation depth with that predicted by Keldysh theory. This opens up a novel method for real-time non-invasive crystallography of crystalline materials.

Acknowledgements

These experiments were done as a partnership between myself, and Sean Kirkwood at the National Research Council Canada. Sean designed and developed the experimental apparatuses and was highly involved in the 3100nm experiments. Further Collaborators on this projects were Dennis Klug, who created the theoretical band-structure simulations for GaAs. Also, Olivier Chalus and the team at the Institut de Cincies Fotniques (ICFO) who developed and maintained the 3 micron laser source used in these experiments.

I would like to thank my supervisor Paul B. Corkum for his insight and support for these experiments. He provided invaluable discussion and inspiration to this project. I give a special thanks to my coworker Sean Kirkwood. He taught me an enormous amount about general research and showed me first-hand how to create and conduct experiments.

Further, I would like to thank the National Research Council Canada for the facilities which were used for conducting the majority of the experiments. I also thank the University of Ottawa for providing me the opportunity to learn and for honouring me with this Masters degree. I would also like to thank the Natural Sciences and Engineering Research Council of Canada (NSERC) for their funding throughout my studies and research.

Finally, I thank my husband, Carlos Trallero for his endless support throughout this process. His encouragement and advice can not be appreciated enough. Without him, I would not have been able to finish this project.

Contents

List of Tables

List of Figures

Chapter 1

Introduction

1.1 Motivation

Atomic, molecular, and optical (AMO) physics has exploded in the last few decades as a tool for studying the fundamental behaviour of matter. Through use of ultrafast laser-atom interactions, we can get a picture into the structure and dynamics of materials. Typically, these experiments are performed on single atoms and molecules by means of directing femtosecond lasers into low density gases in large vacuum chambers. Very little work, both experimentally and theoretically, has been done on studying the behaviour of atoms and molecules in the solid state regime. New technological developments of the laser are now opening up new means of studying solid materials. By delving into solid-state materials, we create a means of developing practical AMO applications in photonics.

In the molecular regime, it was predicted that the multiphoton ionization with a laser depends on the electron distribution about the nucleus. Thus measuring the ionization rate as the laser field is rotated about a molecular orbital axis is like measuring a current as a scanning tunnelling microscope tip is scanned across a surface [16, 24]. This was later shown experimentally by Pavičić *et.al* [20] in CO_2. In Fig.1.1, we show the experimental and theoretical ionization yield for CO_2 as taken from [20]. Both the experimental (dark points) and theoretical data (red line) describe the ionization yield and is plotted as a function of angle between the laser polarization and the constant alignment of the CO_2 molecule. The highest occupied molecular orbital (HOMO) of CO_2 is shown in the centre of the figure. As can be seen, the ionization yield follows the shape of the HOMO. Thus the laser can take a "picture" of the static electron orbital.

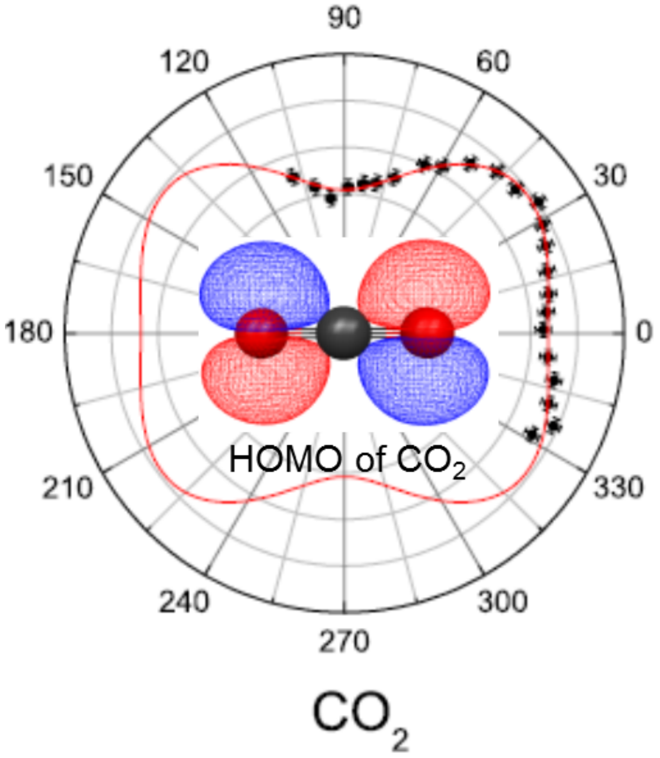

Figure 1.1: Coulomb Explosion Imaging (CEI) results show that ionization yield follows the shape of the highest occupied electron orbital (HOMO) for CO_2 [20]. The dark points and red line represent the experimental data and experimental fit respectively.

In a solid, such as a dielectric or semiconductor, the bandgap (E_g) is on the order of 1-10 eV, which is similar to the ionization potential (I_P) of 8-15eV for an atom or molecule. Thus, we would expect *ab initio* that the multiphoton conduction to valence band transitions within a solid should also depend on the electron distribution in a unit cell. Further, we show that the multiphoton ionization behaviour for both atoms and solids are treated in a similar fashion [13]. Thus, multiphoton ionization inside a solid should also trace the electron distribution.

1.2 From Atoms to Solids

In the case of solids, the electrons are confined within a bulk, so we will use the term "ionization," to refer to multiphoton transitions from the valence bands to the conduction bands. A direct comparison can be made between an orbital in an atom or molecule and an energy band structure in a solid in that they both refer to the electronic distribution about the nucleus.

Immediate differences arise when moving from atoms to solids. We can not use the typical techniques of measuring ionization for molecules, where the ionization byproducts, such as electrons, ions, or high-harmonic generation, are released and caught by a detector. In solids, any ionization byproducts are confined within the solid. However, solids have significantly higher densities than molecular gases (5×10^{22} cm^{-3} versus 3×10^{10} cm^{-3} respectively). Therefore rather than looking at changes in the material, we develop experiments which look at changes in the laser beam itself. These types of experiments are developed by looking at the transmission changes of the laser through the material. The decrease in transmission can be linked directly to depletion of the laser beam due to nonlinear absorption.

1.3 Previous Work

Preliminary experiments looking at multiphoton ionization in dielectrics were performed by Gertsvolf *et.al.* [10]. In these experiments, several dielectrics were ionized with an 800nm laser beam, and the transmission through the sample as a function of crystal-polarization angle was observed. The transmission was modulated with the exact symmetry of the crystal being ionized. The upper portion of Fig.1.2 shows the Fourier transform of the modulation amplitude for three crystals: α-quartz, sapphire (Al_2O_3), and LiF, as a function of crystal symmetry. In other words, having an x-fold symmetry means that the modulation repeated every 360/x degrees. This allows for easy comparison between the symmetry seen in the modulation and the symmetry of the corresponding crystal shown in the lower portion of Fig.1.2.

For LiF (plot c) of the figure), we see a definite four-fold symmetry in the transmission modulation, which reflects the cubic structure of crystal. In the case of α-quartz and sapphire, there appeared two symmetries, the six-fold symmetry of the crystal and an additional two-fold symmetry. The two-fold symmetry was attributed to the birefringence seen by the peripheral field wavevectors, due to the tight focusing. As well, the half-waveplate used to rotate the laser polarization, had a small wedge and hence did not create consistent laser amplitude when rotating. The two-fold symmetry was shown to be independent of the structure in that its effect increased as the laser focal spot travelled through the medium, while the six-fold symmetry modulation depth remained constant in sample depth.

In these experiments, the beam was tightly focused with a small laser power in

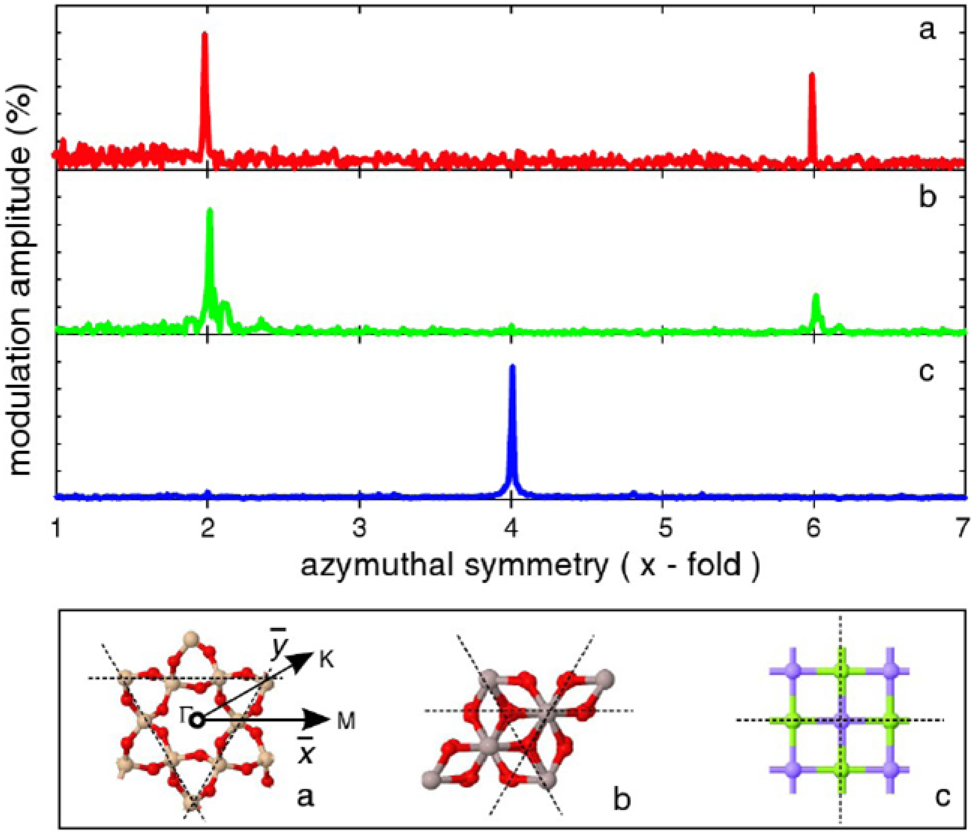

Figure 1.2: Transmission modulation Fourier transform symmetries for various dielectric materials; a) α-quartz, b) Sapphire (Al_2O_3), c) LiF [10]. The modulation scale for a), b) is 0-0.75%, and for c) it is 0-1.5%.

order to avoid self-focusing effects. Thus the symmetries were not visible by eye, due to a low signal to noise ratio, thus requiring the discrete Fourier transform.

The modulation of the laser transmission as a function of crystal angle was linked to a changing ionization rate inside the sample. This is attributed to the variation in the bandstructure shape, specifically the band curvature, which defines the carrier effective mass. The phenomena were specifically linked with characteristics of tunnelling ionization [10]. This notion works only in the assumption that the bandstructure is parabolic near the band minimum, giving a constant and definitive effective mass. This is not the case in dielectrics, which tend to have overly complicated bandstructures that are difficult to interpret. Nonetheless, the experiment shows promising qualitative results and needs to be simplified in order to understand the multiphoton process and make more accurate theoretical predictions.

1.4 Goals

The main goal in this thesis experiment is to show that the powerful techniques developed in AMO physics can now be applied to the solid-state regime. Specifically, we will show that strong-field ionization of solids can be used to trace the electronic structure of the material. We will do this by rotating a GaAs crystal with respect to an infrared laser polarization, as will view the outgoing laser transmission. We will compare the modulated transmission to what is predicted by current nonlinear ionization models, using the effective mass with changing angle. The simplified bandstructure of GaAs allows us to find more accurate effective mass values through simulations using Density functional theory. Also, by choosing a material with a small bandgap, we are able to push the experiment further into the tunnelling ionization regime by using a longer wavelength laser.

By doing this experiment, we develop a new method of crystallography, which is completely nondestructive and can be performed in the bulk and in real-time. We use the term, crystallography, to mean measuring the crystal symmetry and defining the crystal axis. Up to this point, crystallography experiments are performed by x-ray diffraction which both destroys the sample and takes substantially longer to perform.

Chapter 2

Sample Material

In the experiment outlined in this thesis, we must choose a sample material that will allow for comparison with physical theories, but also be common enough for practical applications. We choose GaAs for all the experiments shown here. First we outline the physical properties of the material and why we have chosen this particular material. Then we look at the electronic bandstructure of GaAs and retrieve the effective mass, which will be used in predicting the theoretical ionization rate.

2.1 GaAs

GaAs is chosen for experiments for several reasons. First, GaAs is a common and well-studied III-V semiconductor. GaAs has a high electron mobility which leads to its prominence in electronics and opto-electronics devices. GaAs can be easily polished and machined along specific crystal planes. Second, GaAs has a simple, direct, and parabolic bandgap. The bandgap of GaAs is 1.43eV, which is transparent in the infrared regime. We use lasers at λ=1900nm and 3100nm so we can achieve multiphoton ionization (3 and 4 photon absorption respectively). Thus, we can eliminate any effects of two-photon absorption due to the sharp cutoff at $2\hbar\omega$. Third, GaAs is not birefringent when propagating along a principal axis and thus should not induce any additional symmetry. GaAs is a non-centrosymmetric material meaning that there exists a $\chi^{(2)}$ susceptibility. However, the propagation direction used in the experiments is along the [100] axis of the crystal (as shown in Fig. 2.1), for which the crystal appears non-birefringent. Therefore, it is impossible to achieve phase matching to create an efficient second-order nonlinear process.

We summarize relevant properties of GaAs in table 2.1. All properties are given

Table 2.1: GaAs Properties

	1900nm	3100nm
Bandgap @ 300 K [14]	1.43eV	
Linear Refractive Index, n_0 ‡	3.3697	3.334
Reflection Coefficient ‡	0.2941	0.2900
Absorption Coefficient, α (3μm, 297 K) [15]	2.5 cm^{-1}	
Nonlinear Index, n_2 [6]	3.3 $\times 10^{-13}$cm^2/W	
Thermal Conductivity [15]	0.55 ° C $^{-1}$W cm^{-1}	
Electron Carrier Mobility [6]	8000 cm^2/Vs	
Lattice Constant, a [14]	5.65 $\AA$	

at room temperature at which all the experiments were performed. Sellmeier coefficients are used in any necessary derivations and are shown in Appendix A. The bandgap decides the laser wavelength necessary for transmission. The linear index is used in theoretical calculations of ionization rate and by having the material non-birefringent makes experiments more straightforward. The reflection coefficient is taken into account when calculating the laser energy and intensity inside the sample. GaAs has negligible linear absorption at infrared wavelengths, which means that we can disregard all linear absorption effects. In addition, since the experiments outlined are for 3-photon absorption or above, we can also disregard all two-photon absorption effects. Next, the nonlinear index is responsible for potential self-focusing effects in the sample which will be discussed in section 4.1. Further, we see that the thermal conductivity is low. Together with the heat capacity (0.33 J g^{-1}K^{-1}) and density (5.32 g cm^{-3}), we use the two-temperature model to find that during the course of the laser propagation, the sample temperature only increases by 3 K. This is not enough to create significant temperature-dependent changes to the bandgap. According to heat diffusion equation, the additional heat will dissipate to e^{-2} its initial value in $\sim 300\mu$s, compared to the laser repetition rate of 2 ms. Because of the high electron carrier mobility, in addition to the electrons not being depleted from the sample, the electrons quickly replenish between laser pulses. Finally, the lattice constant is used in converting between real and reciprocal space when analyzing bandstructures.

GaAs has a face-centred cubic (FCC) zinc-blende structure as shown in Fig.2.1. The structure space group is F$\bar{4}$3m. The black and white spheres in the figure are the gallium and arsenic atoms respectively. The zinc-blende structure can be viewed as two FCC structures of different atoms overlapped and displaced by a quarter unit cell. Since it is a cubic structure, it has a four-fold symmetry, and the angles of the unit cell are all at 90°. Fig.2.1 is viewed along the (100) plane, which can be seen as parallel to the $i - j$ axes and normal to the k axis. Due to the cubic crystal structure, the (100) plane is identical to the (010) and (001) planes. The crystal axes, as labelled with the straight brackets, [ ], are normal to their respective planes. The GaAs structure has been predicted through numerous crystal structure prediction (CSP) methods [25] and verified through experimental x-ray diffraction.

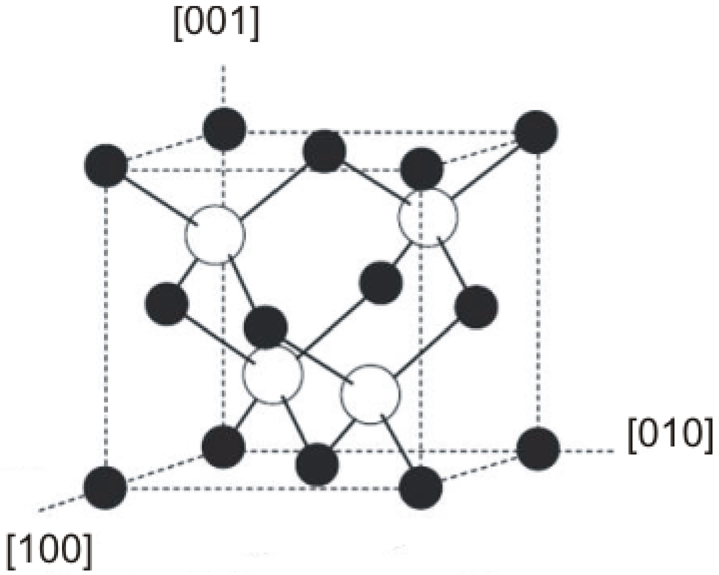

Figure 2.1: FCC cubic structure of GaAs as viewed along the [100] axis. The black and white spheres represent the Gallium and Arsenic atoms respectively.

2.2 GaAs Bandstructure

A major reason for choosing GaAs is the direct bandgap as shown in Fig.2.2. The bandstructure can be described by a parabolic function, near the bandgap. This is important since we will assume a parabolic shape in the band structure when defining the effective mass.

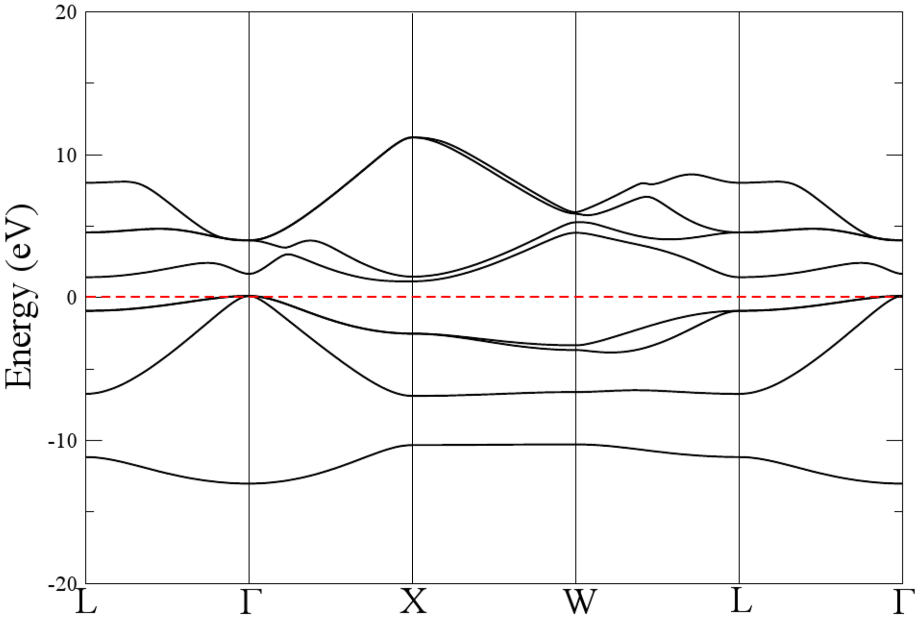

Figure 2.2: Bandstructure of GaAs at P = 0 kPa, as found through density functional theory and ABINIT (created by D. Klug).

In Fig. 2.2, we show the standard view of a crystal bandstructure. The numerous lines represent the energy bands in the solid and are plotted as a function of momentum, $k = p/\hbar$. Zero energy represents the top of the valence bands. All bands below zero energy (red dotted line) are valence bands, for which the first three starting from zero are known as the heavy hole, light hole, and split-off hole bands respectively. All bands above zero energy are conduction bands. The space between the highest valence band and the lowest conduction band is the bandgap. The momentum points, Γ, X, K, L, are the high symmetry points. The valence band edge (energy = 0) occurs at $k = 0$, which is labeled Γ. The point X is located at $k = \frac{2\pi}{a}(100)$ and L is located at $k = \frac{2\pi}{a}(\frac{1}{2}\frac{1}{2}\frac{1}{2})$.

Another useful method to visualize the GaAs bandstructure is with the first Brillouin zone in Fig.2.3. The first Brillouin zone is described in reciprocal space (or momentum space) and plotted in terms of the momentum axes, k_i. The Γ point is the origin and has zero momentum. For the figure shown, the boundary sits at a momentum of $k_i = 2\pi/a$. It describes the primitive cell in reciprocal space, which is unique to the material. The high symmetry points (Γ, X, W, L) can be visualized more clearly and all lie on the boundary. This description is commonly used in solid state physics because it allows for easier study of crystals especially with respect to scattering etc. The GaAs reciprocal lattice seen in Fig.2.3 has a four-fold symmetry,

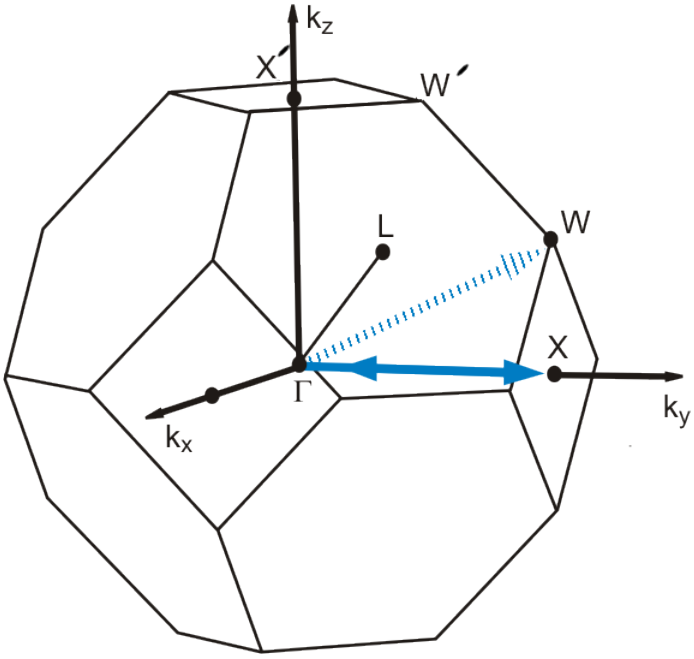

Figure 2.3: GaAs reciprocal lattice (first Brillouin zone) . The propagation axes are marked as k_i. The high symmetry points are labelled Γ, X, W, L.

which is analogous to the GaAs real-space lattice. Due to the direct conversion between the spaces, the laser can be visualized as propagating along direction, k_i, where i can be any of x, y, z due to the symmetry. The polarization of the laser rotates in a plane perpendicular to the propagation.

For our experiments, the bandstructure between high symmetry points is not sufficient. We need to know what bandstructure is seen along the laser polarization direction, as it rotates about the propagation axis. To do this, we model the GaAs bandstructure along changing propagation angles using ABINIT [1]. Here we calculate the structures using density functional theory (DFT) with pseudopotential functions. These simulations were conducted by D. Klug. Fig.2.4 shows the bandstructure for the first section of the Brillouin zone (from X to W). The bandstructure can be envisioned as moving in and out from the central point, Γ; first to point, X and then in multiple incrementing points, Z_i in increasing angle about propagating axis, k_x. Points, Z_i are in reciprocal space and are converted into real space as shown in Appendix B in order to find the corresponding real-space angle. We show only the varying bandstructure between points, X and W in Fig. 2.4. Similar curves are made for the rotation from W to W', and W' to X'. Due to the four-fold symmetry, we found that the pattern repeated for all additional quadrants.

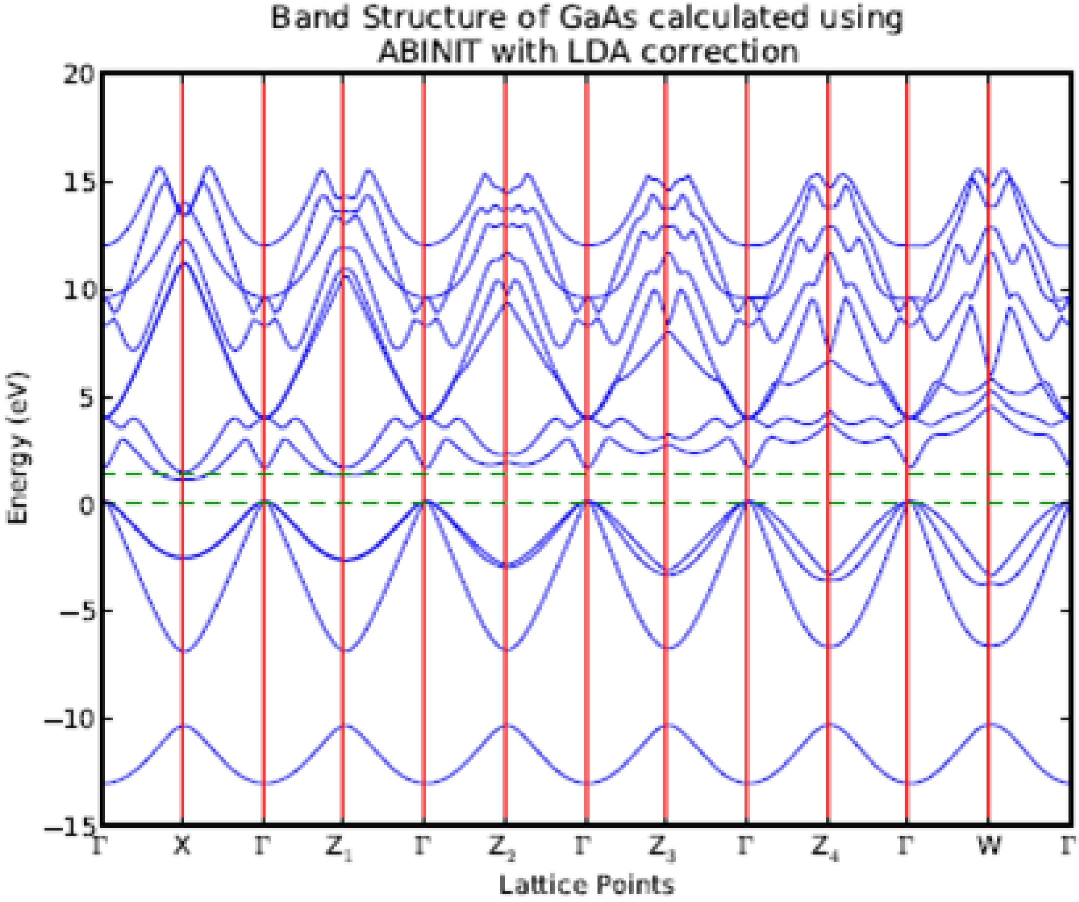

Figure 2.4: Bandstructure for increasing sample angle about the [100] propagation axis, from X to W, as calculated using DFT. Green dotted lines highlight the bandgap.

By looking at the bandstructure in Fig.2.4, we see that there are again multiple energy bands both above and below the bandgap and at first glance, the bandstructure initially does not look simple, as our goals would hope. However, although ionization is possible from numerous valence to conduction bands pairs, the ionization rate decreases nonlinearly with increasing band energy, as a greater number of photons is required to excite the electron. Thus ionization is most probable between bands close to the bandgap. So we will focus on the first conduction, and the first two valence bands (heavy hole and light hole), making the bandstructure easier to interpret.

We then look at the density of states (DOS) for each of these bands, which is estimated by;

$$DOS = \frac{1}{V}\left(\frac{d\varepsilon}{dk}\right)^{-1} \tag{2.1}$$

where V is the volume of the unit cell, ε is the band energy and k is the reciprocal lattice vector (adopted from Kittel [14]). The DOS from the DFT bandstructures is calculated by taking the first derivative using the Savitzky-Golay method [22] combined with eqn.(2.1). The DOS for the X symmetry point is calculated by S. Kirkwood and shown in Fig.2.5.

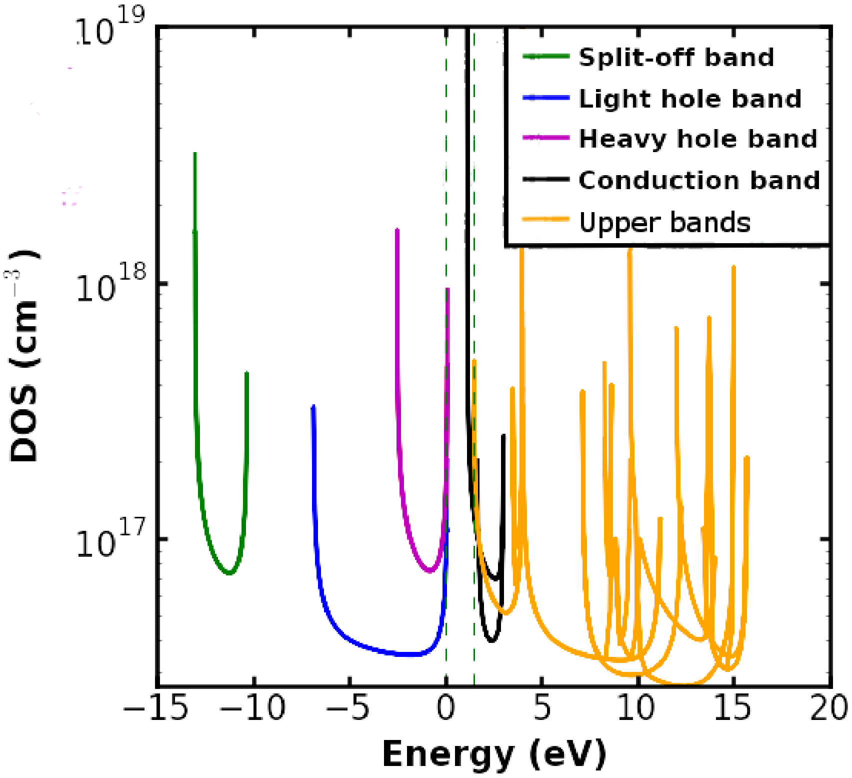

Figure 2.5: The density of states for the X symmetry point in GaAs calculated by density functional theory. The green dotted lines highlight the bandgap.

Each coloured curve corresponds to a different energy band in the bandstructure. The energy on the azimuthal axis directly corresponds to the energy levels of the bandstructure plots ordinate axis. The vertical dotted green lines are located at the bandgap. The DOS describes the density of electrons available for ionization at each energy band. If a curve in the bandstructure is flat, then the density of states will be much higher since more electrons can exist at the same energy. The density of states for the heavy hole band is higher than for the light hole, as seen in Fig.2.5, which means that there are significantly more electrons in the heavy hole band available for ionization.

2.3 Effective Mass

As will be described more thoroughly in chapter 3, the ionization rate inside a semiconductor, depends on the effective mass of the material. The effective mass is the apparent mass of an electron inside a solid as if behaving according to the dynamics equation, $F = (m^*)a$, where F, a, and m^* are the force, acceleration and effective mass respectively. By writing $\vec{F} = \hbar \frac{d\vec{k}}{dt}$ (see full derivation in [14]), we define the effective mass as,

$$m^* = \hbar^2 \left(\frac{d^2 \varepsilon}{dk^2} \right)^{-1} \tag{2.2}$$

where ε is the band energy and k is the lattice vector. From the bandstructure in Fig.2.4, there are two techniques to retrieve the effective mass. First, the curves near the bandgap are fit with a parabolic curve, from which the second order coefficient can be found and used to find m^*. However, this method runs the uncertainty of choosing the proper number of points about the band edge to fit. The value of effective mass can change by nearly four times depending on the number of points chosen. The second method takes the second derivative of the bandstructure, using the Savitzky-Golay method [22] to find m^*. This method provides results very similar to those seen in literature, as seen in table 2.2, and thus is the preferable choice.

The effective mass is calculated for each band at the Γ point. Since the GaAs lattice has a four-fold symmetry as seen in Fig.2.3, the effective masses calculated from point, X to point W (first quadrant) can be repeated for the other three quadrants. The effective masses are plotted as a function of real space angle between the crystal and laser polarization, for the conduction and valence bands in Fig.2.6. The effective mass is plotted as a ratio of the free electron mass. The absolute values of the masses are shown. We show the masses for a laser propagating along the [100]

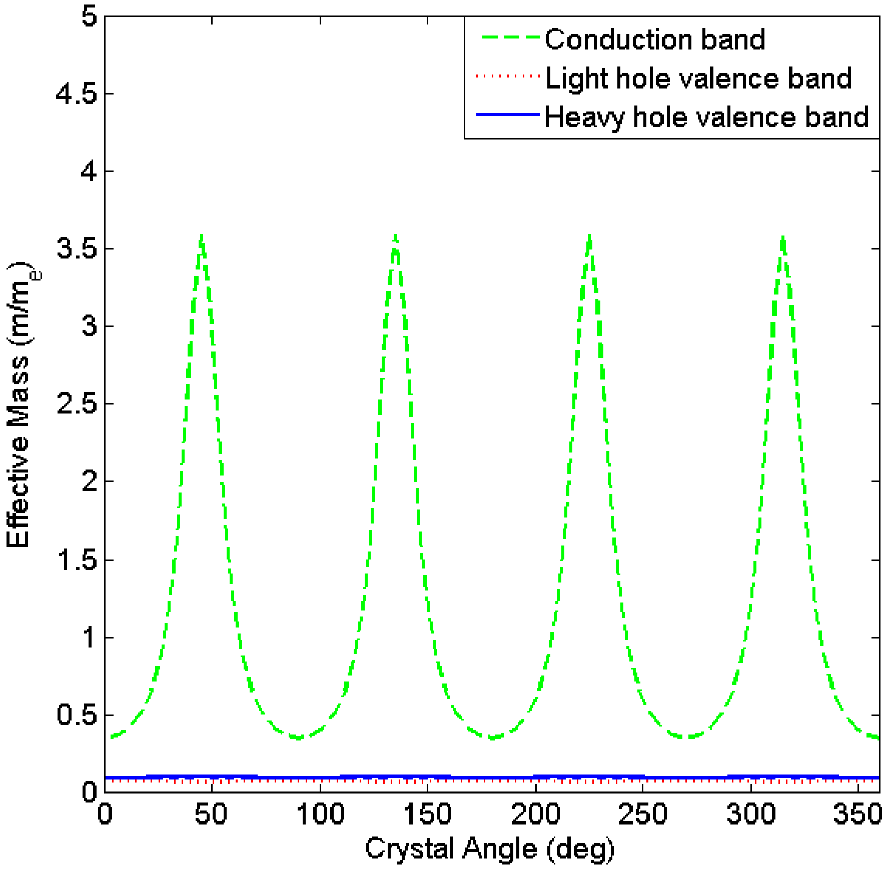

Figure 2.6: Effective mass of the lowest conduction band and two highest valence bands in GaAs. The effective masses are calculated using DFT and are plotted as a function of the relative angle between the crystal and laser polarization.

axis, which is perpendicular to the (100) plane. Thus the azimuthal crystal angle is the angle between the laser polarization and the [001] axis. So at 0°, the polarization is aligned along the [001] axis, and at 90°, the polarization lies along the [010] axis. Due to symmetry, the same curves would arise if the laser propagates along either the [010] axis or [001] axis. The conduction band effective mass is much higher and has the same phase as the heavy hole valence mass. The light hole valence band mass is shifted by 90°. All masses are modulated and repeat with a four-fold symmetry. In fact, this is a clear way of showing the repetitive nature of the GaAs bandstructure, since the effective mass is defined by band curvature.

Table 2.2: Carrier effective mass for GaAs along direction Γ to X

	m^*	
Band	DFT	tabulated [15]
Split-off	1.167	0.17
Light Hole	0.074	0.082
Heavy Hole	0.345	0.50
Conduction	0.068	0.066

In ionization, the electron is excited from the valence band to the conduction band and so the ionization rate depends on the curvature of both these energy bands. So we use the reduced effective mass for all theoretical predictions, as defined by,

$$\frac{1}{m_r} = \frac{1}{|m_c^*|} + \frac{1}{|m_v^*|} \tag{2.3}$$

where m_v^*, m_c^* is the effective masses of the valence band and conduction band respectively. For the purposes of ionization, the absolute value of the mass is used. The sign of the mass infers directionality of the carrier acceleration. However, ionization rate does not depend on the motion of carrier motion after ionization. In addition, the valence mass refers to a hole mass, rather than an electron mass, which always travels in the opposite direction of an electron.

The reduced mass using the heavy hole and light hole bands are shown in Fig.2.7. In this figure, the effective mass is plotted as ratio of the free electron mass. We show the absolute value of the mass as a function of the GaAs crystal angle. First we note that the light hole reduced mass varies with a smaller amplitude than the heavy hole mass. This will become important when discussing ionization rates for these bands. More importantly, the phase of the two curves is shifted by 90° with respect to each other. We will show that the laser transmission is related to the reduced effective mass and thus the transmission modulation phase will reflect the band from which it ionizes.

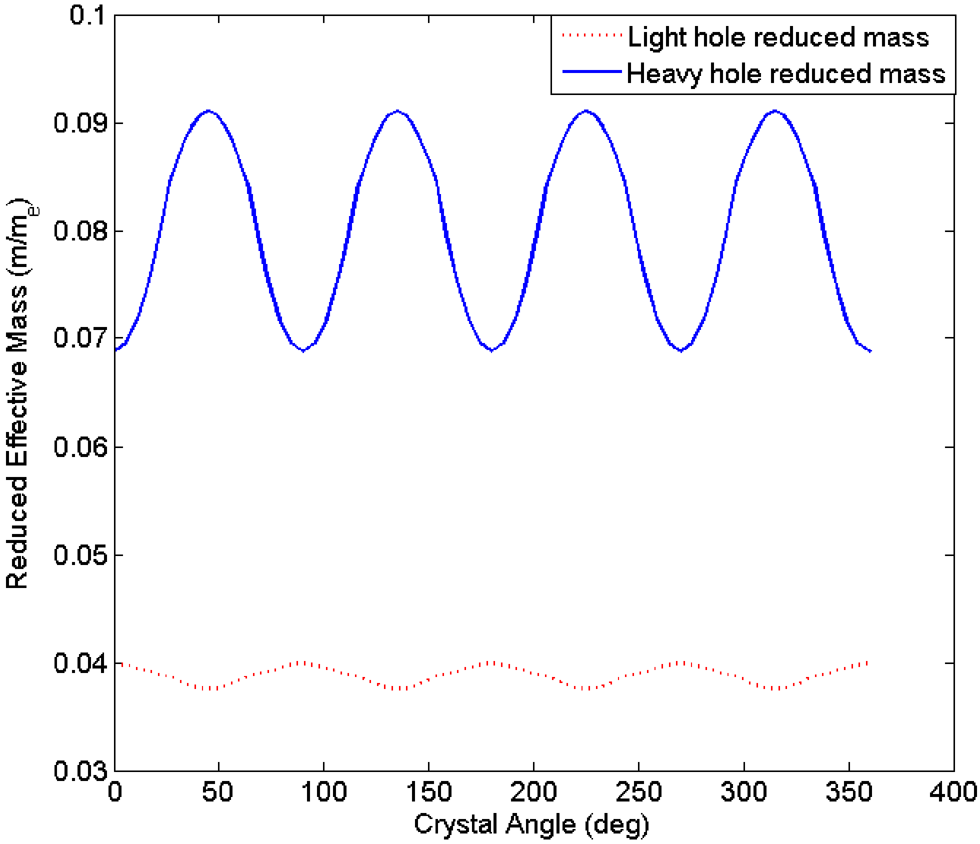

Figure 2.7: Reduced effective mass of GaAs as calculated using derivatives of DFT bandstructure.

Chapter 3

Theory

In this chapter, we look at the theoretical multiphoton ionization rate in solid materials. We use a Keldysh ionization theory in solids for all predictions. We first address why this particular theory is chosen. Then we describe the mathematical equations of the theory and the different regimes of its behaviour. We then utilize the theory in predicting theoretical transmission and modulation values in GaAs.

3.1 Ionization in Solids

In the previous work done by Gertsvolf *et. al.*[10], the ionization behaviour in dielectrics was described using Zener tunnelling [17].This model uses a quasi-classical approximation (WKB). The ionization rate is found by solving the Schr*ö*dinger equation and Bloch indices, assuming two parabolic energy bands (conduction and valence). The ionization rate is given as,

$$w(F) \propto \exp\left[-\frac{(2E_g)^{3/2}\sqrt{m^*}}{3e\hbar F}\right] \tag{3.1}$$

where w is the ionization rate, E_g is the bandgap, $\sqrt{m^*}$ is the effective mass, and F is the electric field. Zener tunnelling can be visualized by an electron sitting at the top of a single parabolic valence band. The conduction band is lowered in energy by an electric field until its lowest energy equals the top of the valence band energy. If the electron can jump over a distance of E_g/eF, then it tunnels into the conduction band without any change of energy. This model is limited due to several reasons. First, the model assumes that the lowest energy of the conduction band coincides with the highest valence band energy in momentum space. That is, Zener only uses two parabolic bands and neglects the more complicated band structure in multiple directions, and allows only electron transitions along the same momentum. More commonly, the transition energy of the electron is higher than the theoretical bandgap. Therefore, Zener underestimates the electric field strength to ionize [12]. Second, Zener only describes the tunnelling regime of multiphoton ionization, but does not describe details of the perturbative multiphoton ionization regime. In addition, the effective mass is not clearly defined in eqn.(2.3), as to which mass is being used (whether conduction or valence). The effective mass of the conduction and valence bands will be different and ionization will depend on both. In the work done by Gertsvolf *et. al.*[10], the Zener model was used with the reduced effective mass in dielectrics. They found that a general trend relating the ionization rate (and transmission modulation) could be made, despite the non-parabolic nature of the dielectric bandstructure. However, the theory was unable to predict numerical values in these materials.

L. V. Keldysh developed a more rigorous ionization model in 1965 [13], which derives the average probability of ionizing a valence band electron into the conduction band over a time greater than the period of the electric field, $2\pi/\omega$. This is provided that the frequency of the electric field is not close to any resonances; thus transparent to the field. Keldysh treated solids in a similar manner to his theory for ionization of atomic gases, which he wrote in the same paper. Since then, many additional paper have been written to further describe the strong-field ionization in atoms and molecules [4, 21]. However, little theoretical work has been advanced in the field of strong-field ionization in solids. Therefore, we will be using the current Keldysh theory for ionization to model our results.

The Keldysh theory in solids uses the Bloch wave functions which contain periodic functions, having the translational symmetry of the crystal lattice. The ionization transition is treated as a single-electron problem, but accounts for dispersive behaviour; thus an effective bandgap is defined. The probability is found for direct transitions, summing over all multiphoton processes (photon energies, $n\hbar\omega$) for $n = -\infty$ to ∞, for a single energy band. The reduced mass as defined in eqn.(2.3) is used in the calculations.

Keldysh divides ionization into two different regimes; perturbative multiphoton ionization (MPI) and tunnelling ionization. In the MPI regime, the electron absorbs multiple laser photons to excite from the valence band to the conduction band. In the tunnelling regime, the energy bands are suppressed by the laser electric field allowing the electron to tunnel from the valence band, through the potential barrier into the conduction band before the electric field reverses the sign of the potential. This only occurs if the laser frequency is slower than the mean-free transit time of the electrons. To determine which ionization regime is occurring, Keldysh introduced a frequency-normalized parameter for solids, known as the Keldysh parameter;

$$\gamma = \omega \frac{\sqrt{E_g m^*}}{eF} \tag{3.2}$$

where ω, E_g, m^*, and F are the angular frequency, band gap, effective mass, and field strength respectively. In the limit $\gamma \ll 1$, multiphoton ionization is described by tunnelling. If $\gamma \gg 1$, then multiphoton ionization is determined by perturbation theory. This Keldysh parameter for solids defers from the atomic case by a factor of $1/\sqrt{2}$.

First we look at Keldysh ionization theory in the two limits. Then we will write the full expression. In the tunnelling regime ($\gamma \ll 1$), the Keldysh ionization rate can be written in terms of γ, as

$$w_{Tunnel}(\gamma) = \frac{2}{9\pi}\frac{E_g}{\hbar}\left(\frac{m^* E_g}{\hbar^2}\right)^{3/2}\left(\frac{\hbar\omega}{E_g}\frac{1}{\gamma}\right)^{5/2}\exp\left\{-\frac{\pi}{2}\frac{E_g}{\hbar\omega}\gamma\left(1-\frac{1}{8}\gamma^2\right)\right\} \tag{3.3}$$

From this equation (adopted from [13]), we immediately see that the tunnelling regime completely breaks down when $\frac{1}{8}\gamma^2 > 1$ or $\gamma > 2.8$. This is because, we expect that the ionization rate will increase with increasing intensity, and thus should decrease with γ.

As $\gamma \gg 1$, the rate enters the perturbative multiphoton regime (MPI) and the expression becomes,

$$\begin{aligned} w_{MPI}(\gamma) = \frac{2}{9\pi}\omega\left(\frac{\omega m^*}{\hbar}\right)^{3/2} & \Phi\left[\left(2\left\langle x+1\right\rangle - 2x\right)^{1/2}\right] \\ \times\exp & \left\{2\left\langle x+1\right\rangle\left(1-\frac{1}{4\gamma^2}\right)\right\}\left(\frac{1}{16\gamma^2}\right)^{\langle x+1\rangle} \end{aligned} \tag{3.4}$$

where $x = \tilde{\Delta}/\hbar\omega$, Φ is the Dawson integral, the brackets $\langle\rangle$ represents the integer portion, and $\tilde{\Delta}$, is the effective bandgap energy. In the MPI regime, the effective bandgap can be written as,

$$\tilde{\Delta} = E_g + \frac{e^2 F}{4m^* \omega^2} \tag{3.5}$$

Due to the γ dependence, we can see that the Keldysh equation is field strength-dependent, and hence intensity dependent for all regimes. In these sets of experiments, the intensity range spans both the MPI and tunnelling regimes. Thus we use the full Keldysh theory as outlined in [13]. First, we introduce the following simplifying expressions:

$$\begin{aligned}
\gamma_f &= \frac{1}{\sqrt{1+\gamma^2}} && (3.6)\\
E_1 &= E\left(\gamma_f\right) && (3.7)\\
E_\gamma &= E\left(\gamma\gamma_f\right) && (3.8)\\
K_1 &= K\left(\gamma_f\right) && (3.9)\\
K_\gamma &= K\left(\gamma\gamma_f\right) && (3.10)
\end{aligned}$$

where E and K are elliptic integrals of the first and second kind. In general, the effective bandgap is,

$$\tilde{\Delta} = \frac{2E_1}{\pi\gamma\gamma_f} E_g \tag{3.11}$$

The bandgap appears to increase with increasing laser intensity. Using the expressions in eqn. (3.6), we rewrite eqn.(37) in Keldysh's paper [13], as

$$w(\gamma) = \frac{2\omega}{9\pi}\left(\frac{m^*\omega}{\hbar\gamma\gamma_f}\right)^{\frac{3}{2}} Q\left(\gamma, \frac{\tilde{\Delta}}{m^*\omega}\right) \exp\left\{-\pi\left\langle\frac{\tilde{\Delta}}{\hbar\omega}+1\right\rangle\right\} \frac{K_\gamma - E_\gamma}{E_1} \tag{3.12}$$

where the function Q is;

$$Q(\gamma, x) = \sqrt{\frac{\pi}{2K_1}} \sum_{n=0}^{\infty} \exp\left\{-\pi n \frac{K_\gamma - E_\gamma}{E_1}\right\} \Phi\left(\sqrt{\frac{\pi^2(2\langle x+1\rangle - 2x + n)}{2K_1 E_1}}\right) \tag{3.13}$$

The index, n, is summed over the multiphoton order. To solve numerically for the full Keldysh ionization rate in eqn.(3.12), the elliptical integrals are first computed along with all values that do not depend on n. Next, the summation of

$Q(\gamma, x)$ is evaluated starting at $n = 0$ and incrementing with the Dawson integral in eqn.(3.13). The summation continues until either the incremental ratio, dQ/Q, is smaller than a predefined tolerance value of 10^{-6}, or the loop has iterated 10^6 times without converging. Then the remainder of eqn.(3.12) is evaluated.

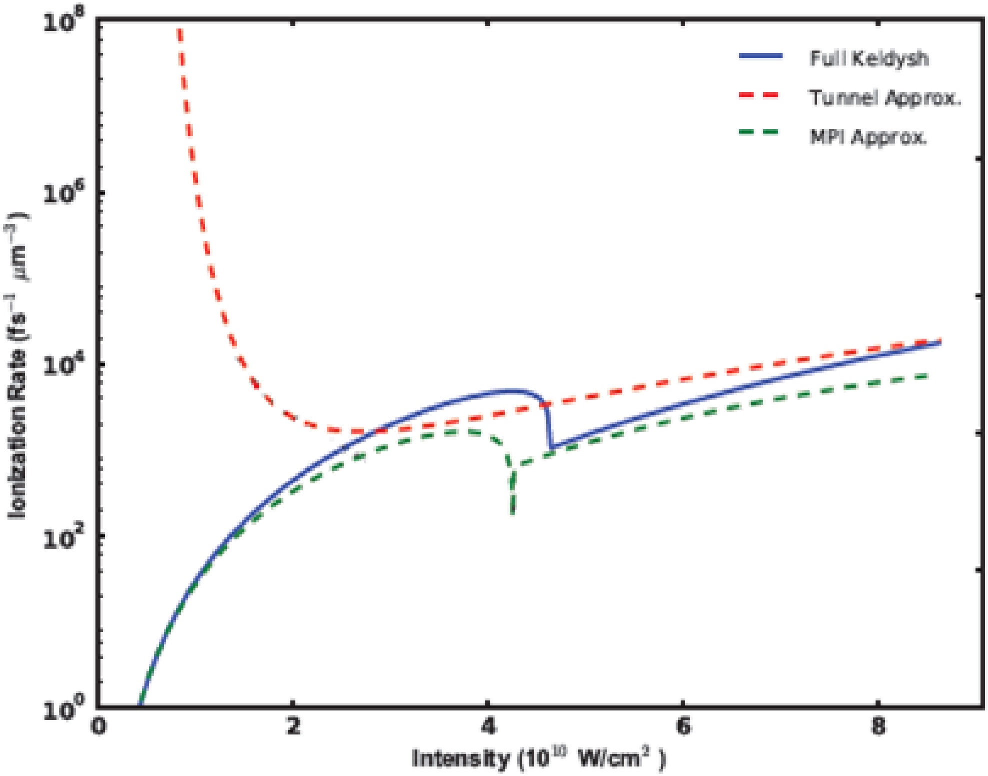

Figure 3.1: Ionization rates in (100)GaAs for different multiphoton ionization regimes for a 3.1 μm laser pulse with a peak intensity in the 10^{10} W/cm^2 range. An effective mass of 0.068m$_e$ is used.

The Keldysh ionization rate is plotted for a reduced mass of 0.068 m$_e$ at the Γ point in Fig. 3.1 for an intensity range $\sim 10^{10}$ W/cm^2. We show ionization in the pure multiphoton and tunnelling regimes in the green and red dotted lines respectively. The blue line shows the full Keldysh ionization curve. Ionization occurs in the MPI regime until an intensity of $\sim 3 \times 10^{10}$ W/cm^2. The pure tunnelling ionization mechanism is not reached until nearly 10^{11} W/cm^2 where the electric field at this wavelength is sufficient to distort the potential barrier for a electron of this mass to tunnel out of the valence band. In between the two regimes limits, we see both the MPI and full ionization rate undergo a dip. This occurs due to channel closing. According to equation, 3.11, the effective bandgap increases with intensity. In GaAs, four photons are necessary for ionization with 3.1μm laser. However as intensity and bandgap increase, a certain intensity is reached where the number of photons necessary for the ionization increases from four to five, causing the ionization rate to drop suddenly. A similar phenomenon occurs for 1900nm, but for a higher intensity. For our experimental intensity range of 2×10^{10} W/cm^2 to $\sim 6 \times 10^{10}$ W/cm^2, it is clear that a full Keldysh equation is necessary in predicting ionization rates.

3.2 Keldysh Ionization inside GaAs

We look at the Keldysh ionization rate inside GaAs by calculating the rate in eqn.(3.12) with the varying effective mass as described in section (2.3). This will be used in predicting the transmission modulation in GaAs. First we begin by re-visiting the heavy and light hole valence bands.

Due to the highly nonlinear behaviour of the ionization, excitation occurs primarily between the bands lying most closely to the bandgap. Ionization depends on the reduced effective mass between the conduction and valence bands. As described in sections (2.2, 2.3), there are light and heavy hole valence bands, which both have the same peak energy at the band-edge. The Keldysh ionization rate using the reduced mass for the heavy and light holes (see Fig. 2.7) as a function of real-space crystal angle is plotted in Fig.3.2. This is the ionization rate of GaAs for a 1900nm laser with a peak intensity of 10×10^{10} W/cm^2. Thus according to Fig.3.1, we are further in the tunnelling regime. We have chosen to plot in this regime since this is the regime of most interest and the intensity in which experiments will be performed. The plot is created by calculating the full Keldysh ionization rate given in eqn.(3.12), using the reduced effective masses shown in Fig.2.7. The crystal angle in the azimuth again refers to the relative angle between the laser polarization and the [001] axis of the GaAs crystal. A deep modulation in the ionization rate is symmetric and repeats itself every 90°. The curve is therefore identical for all angle quadrants. Thus it shows the four-fold symmetry of the GaAs cubic crystal. As ionization rate increases, more photons will be absorbed for a given laser beam and hence transmission will decrease. Thus, the transmission should also be modulated, and will have a four-fold symmetry.

In Fig.3.2, the ionization rate of the light hole valence band is greater than for the heavy holes. In the tunnelling regime, the carrier needs to be accelerated in order to tunnel through the deformed barrier. Light hole carriers will accelerate more than heavy hole carriers and therefore should ionize more readily. However, the ionization rate as a function of angle due to the light holes varies only by 1.3×10^4 fs$^{-1}\mu$m^{-3}, while the heavy hole ionization rate varies by 2.3×10^4 fs$^{-1}\mu$m^{-3}, which is nearly double. So although ionization can be expected from both bands, the modulation in transmission will be due primarily to the variation in the heavy hole effective mass. Next, the phase of the ionization rate for the heavy and light hole bands differs by 90°. As will be seen in the experimental results, the transmission modulation follows the rate predicted by the heavy hole band and not the light hole band.

In this thesis, we perform experiments with two different laser wavelengths: 1900nm and 3100nm. Since the ionization rate depends on the angular frequency, as seen in eqn.(3.12), we look at differences at the Keldysh ionization rate for the two wavelengths of interest. In Fig.3.3, the ionization rate for both 1900nm and 3100nm is plotted as a function of peak pulse intensity inside the sample. We interestingly note that the curves are very similar. However, the 3100nm curve shows the signs of channel closing similar to what was seen before in Fig. 3.1. However, the 1900nm curve does not show any such signs. The reason is that the photon energy for 1900nm is much larger than for 3100nm. So as the effective bandgap increases with intensity for1900nm, the intensity necessary to access the next channel closing is not reached until the ionization moves toward the tunnelling regime, which is out of the range of this plot. This has been seen by extending the intensity range of the simulation.

Simulations of the transmission and modulation depth are made by starting initially with a Gaussian pulse with a given peak intensity, pulse duration, beam radius, and wavelength, specific to each experiment. These simulations will be used to predict all curves specific to our experiments and will compare Keldysh theory to our results, shown in section (5). The pulse is propagated through 600μm GaAs, in increments of dz. In the case of soft focusing, the beam radius is held constant for all points in the crystal. At each dz, the intensity is found for all points in the beam radius, r, and in time, t. From the intensity, we calculate the electric field and Keldysh parameter. The ionization rate is determined for each point (in space and time) using eqn.(3.12), then the number density of electrons ionized is given by,

$$dN = (N_T - N)\ w(\gamma)\ dt \tag{3.14}$$

where N_T is the total initial electron density of the sample and $w(\gamma)$ is the Keldysh ionization rate from eqn.(3.12). This expression takes into account depletion of valence electrons. The relaxation time of the carriers in GaAs is much longer than the pulse duration and hence there is no relaxation/recombination term in eqn.(3.14). The energy absorbed from each point, dz is found by,

$$dE_{abs} = E_g\ N\ 2\pi r dr dz \tag{3.15}$$

which comes from the fact that the change in intensity from each point is $E_g N dz/dt$.

The change in intensity is subtracted from the current intensity for subsequent propagation, to account for laser depletion. The pulse continues to propagate through the entire crystal length of 600μm and the total absorbed energy is summed from all points. The transmission is then defined as,

$$\text{Transmission} = \frac{E_{in} - E_{abs}}{E_{in}} \tag{3.16}$$

where E_{in} is the initial energy of the laser. This process is repeated for all reduced effective mass values of GaAs as predicted in Fig. 2.6. The modulation curve is then retrieved by looking at the variation in the transmission with angle. This entire simulation is done for multiple input peak intensities to use for comparing experiment with theory.

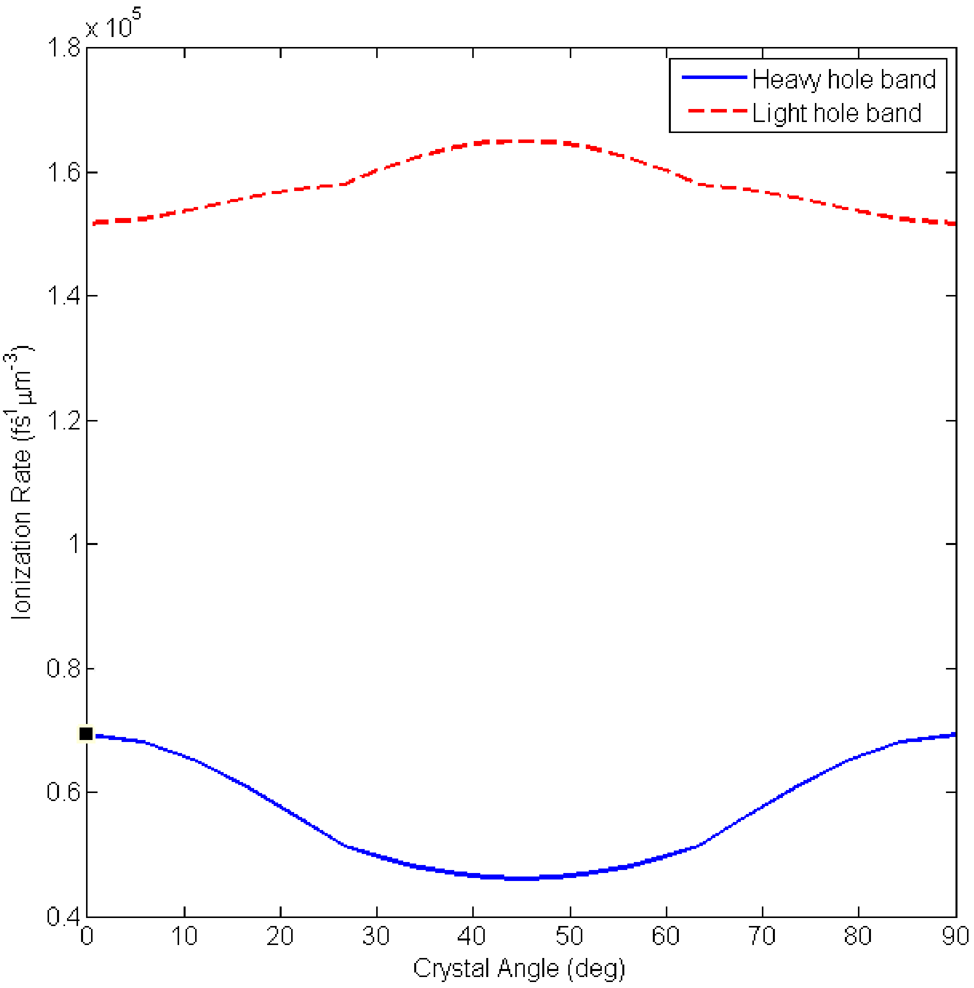

Figure 3.2: Keldysh peak ionization rate for the heavy and light hole bands in (100)GaAs using a 1900nm laser beam. The ionization rate uses the reduced effective mass for the respective heavy and light hole valence bands, and an intensity of 10×10^{10} W/cm^2, when calculating the ionization rates.

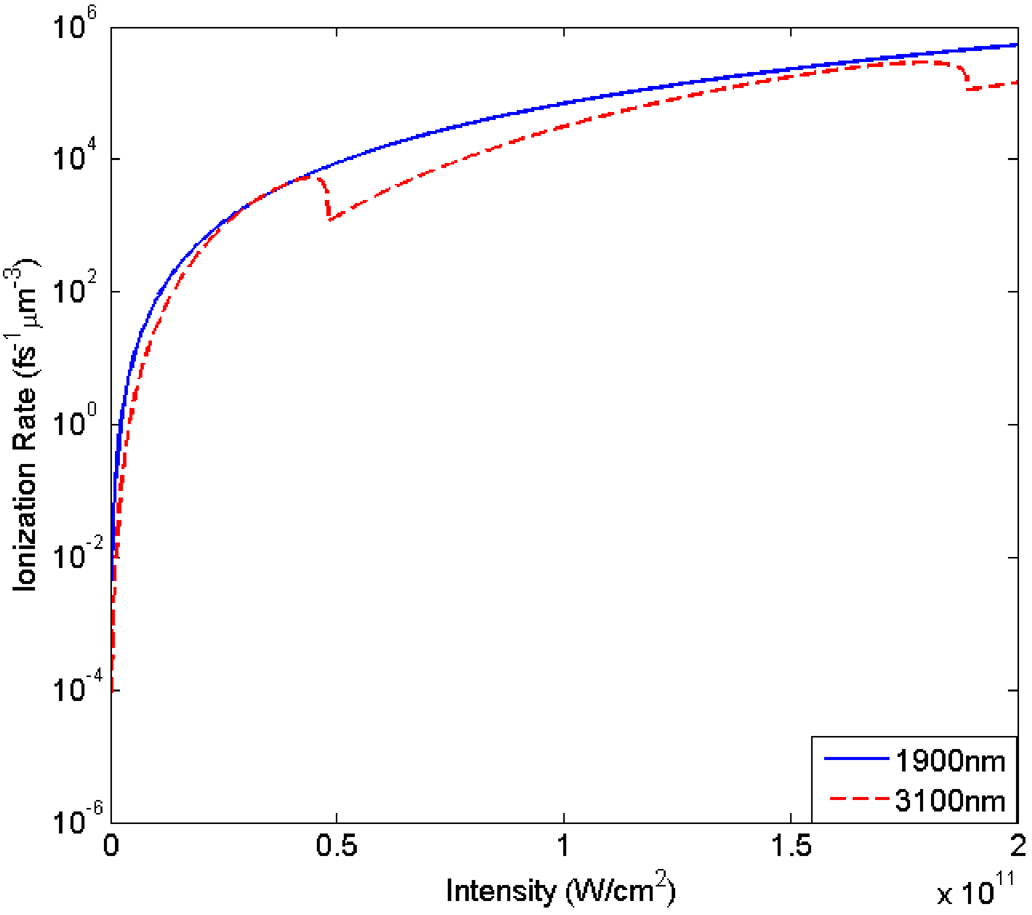

Figure 3.3: Full Keldysh ionization rates in (100)GaAs for 1900nm and 3100nm as a function of peak laser intensity. The rate equation uses the heavy hole reduced effective mass.

Chapter 4

Experiments

In these series of experiments, a 600μm thick sample of (100)GaAs is rotated with respect to the laser polarization. The laser transmission is monitored as a function of angle. Since the bandgap of GaAs is 1.43eV, an infrared beam is required to see transmission. In this thesis, two independent experiments are performed with two wavelengths; 1900nm and 3100nm. The majority of experiments will focus on using a 1900nm laser system, which were performed at the National Research Council Canada. These experiments will be the focus of this thesis. We will also outline the 3100nm experiments, performed at the Institut de Ciences Fotoniques (ICFO). The 3100nm experiments push the ionization further into the tunnelling regime. We show the experimental setup used in the preliminary experiments and discuss future modifications.

In this chapter, we first describe the experimental considerations, including self-focusing and phase advance. We will discuss how the experiment is designed to avoid these nonlinear effects. We then go into detail on the specifications and the setups of the 1900nm and 3100nm laser systems.

4.1 Experimental Considerations

4.1.1 Intensity

When performing these experiments, the key issue is not the exact intensity at which the modulation process occurs, but the trends in transmission and modulation depth that are seen with changing intensity. We begin by determining the threshold ionization of GaAs, which is the minimum intensity for the electrons to transition from the valence to conduction bands. From there, we develop our experimental setup to conform to this minimum intensity.

According to "over-the-barrier" gas ionization theory, the ionization threshold is proportional to the ionization potential as $I_{th} \propto I_p^4$ (see Appendix C) , and is independent of wavelength. The bandgap is analogous to the ionization potential, so we can scale the ionization threshold in GaAs from previous experiments done in quartz (E_g = 9eV, $I_{th} = 1 \times 10^{13}$ W/cm^2) [10]. By this approach, we arrive at an ionization threshold of $\sim 1.6 \times 10^{10}$ W/cm^2 for GaAs (E_g = 1.43eV). Although the intensity at which ionization occurs is not a step function, this intensity can be used as a guideline for the minimum intensity necessary to ionize the material. Typically surface damage in GaAs should not occur until intensities above $\sim 10^{13}$ W/cm^2. This intensity is obviously much higher than the threshold intensity calculated above. Therefore the bulk can be ionized before producing surface damage. Experimentally, this means that we can perform experiments both with the focused or unfocused geometries.

As a first approach, we will calculate the laser intensity using a geometrical approach. The intensity inside the sample can be estimated by assuming a Gaussian beam profile. By starting from the lens, with focal length, f, the minimum beam waist, w_0, inside the sample is,

$$w_0 = \frac{\lambda f}{\pi w_L} \tag{4.1}$$

where w_L is the incoming beam radius before focusing. Both beam radii are measured as 1/e in the field. Experimentally the beam size is measured with a knife-edge and photodiode. The intensity can be found from the incoming pulse energy, by

$$I_{pk} = \frac{2E_{pulse}}{\sqrt{\pi}\pi w_0^2 \tau} \tag{4.2}$$

where τ is the pulse duration, 1/e in intensity. See derivation in Appendix E. Table (4.1) shows the laser parameters of spot size, pulse duration, and focused spot size, and maximum intensity for both laser wavelengths.

While such calculated values of the laser intensity give us a close estimate of the intensity. generally this method is prone to errors, because small fluctuation in beam spot size lead to large variations in intensity. More fundamentally, the beams used in the experiments are not perfect Gaussian curves. Therefore a better estimate of the intensity can be found by fitting the experimental transmission curves to the detailed theoretical model as described in chapter 3. The results of such a fitting can be seen in Fig.5.3. Using this procedure, for the 1900nm experiments, we find that the maximum pulse energy of 6μJ corresponds to a peak intensity of 6×10^{10} W/cm^2. For the 3100nm experiments, the maximum pulse energy is 1.6μJ, which corresponds to an intensity of approximately 2.5×10^{11} W/cm^2 .

4.1.2 Self Focusing in GaAs

Through the intensity-dependence of the linear refractive index, a beam propagating through a material may experience a time-dependent index which will cause the beam to prematurely focus (self-focusing) or defocus. In the case of self focusing, the beam experiences an increase in the refractive index. The intensity-dependent refractive index, n, is given by,

$$n = n_0 + n_2 I(t) \tag{4.3}$$

where n_0, n_2, and $I(t)$ are the linear index, nonlinear index and intensity respectively [6]. In the case of GaAs, the nonlinear index is $n_2 = 3.3{\times}10^{-13}$ cm^2/W. The linear indices for the respective wavelengths can be found in Table (2.1). With the maximum intensity used in experiments, the refractive index change may be as large as 2%. The index change is highest at the beam peak and falls away with the pulse profile, causing the beam to self-focus. Self-focusing will overcome the beam's natural divergence if its power is above a critical power,P_{crit} [6];.

$$P_{\text{crit}} = \frac{\pi(0.61)^2\lambda^2}{8n_0n_2} \tag{4.4}$$

For our (100)GaAs sample, the critical power is 4.8kW for 1900nm. In order to visualize the possible effects of self-focusing in these experiments, we develop two experimental conditions using 1900nm; hard and soft focusing.

In hard focusing, the beam is focused with a 35mm lens which, using eqn.(4.1), gives a focal beam waist of $w_0 = 19\mu$m inside the sample. Using the threshold peak intensity of 1.6×10^{10} W/cm^2, we get a pulse power of 34kW, given that the peak laser power is,

$$P = \frac{I_{pk}\pi w_0^2}{2} \tag{4.5}$$

This is already above the critical power of 4.8kW and thus we would expect self focusing to occur. To keep the laser power below the critical boundary, the beam waist would need to be under 4.5μm. Using eqn.(4.1) the focal length would need to be 8.2mm. Although this focal length may be available, the energy required to reach the GaAs ionization threshold would be 7.4nJ, which is near the noise threshold in our experiment. Thus the hard focusing experiments do not allow for powers below the critical power for self-focusing.

We take a different approach by soft focusing and increasing the focal length to harbour a nearly non-focused state. Rather than try to keep the power below the critical power, the beam is made large so that the change in beam waist due to self focusing will be of negligible effect. Using the maximum allowed energy output of the 1900nm laser system ($\sim 40\mu$J), we choose a focusing lens of 200mm in order to still reach sufficiently above the threshold intensity. This gives a beam waist of 110μm and a pulse power greater than 1MW. The Rayleigh range is 2.0cm which is over 30 times the thickness of the sample, and so the beam size and intensity is nearly constant through the sample. The distance at which the beam will come to a focus is z_{sf} [6].

$$z_{sf} = w_0 \sqrt{\frac{n_0}{2 n_2 I_{pk}}} \tag{4.6}$$

This distance depends on the intensity inside the sample. As the intensity increases, the self-focusing distance decreases. The peak laser intensity is not constant inside the sample, because it undergoes Keldysh ionization. Using eqn.(3.12) and the ionization simulations described in section (3), we model the peak intensity inside a 600μm thick GaAs sample with respect to propagation distance inside the sample in Fig.4.1.2. We start with a peak intensity of 6×10^{10} W/cm^2, because this is the highest possible intensity with the experimental 1900nm pulse using a soft-focusing setup. The pulse enters the sample and undergoes ionization as it propagates and we have plotted the peak intensity of the pulse. The intensity falls to approximately 1/e times its maximum value upon exiting the sample.

To investigate the effects of self-focusing inside the sample, we assume a constant peak laser intensity of 6×10^{10} W/cm^2 inside the sample, which is the worst case scenario. The corresponding self-focusing distance is calculated using eqn.(4.6), which equals 1.4mm. Using simple geometry, we find the exiting intensity has increased by a factor of 1.6, purely due to self-focusing. We compare this value to Fig.4.1.2, where the laser intensity decreases by a factor of 2.9 due to Keldysh ionization. In addition, we note that the self-focusing estimate is based on a constant peak intensity of 6×10^{10} W/cm^2, and will have even less of an effect at lower intensities. Therefore the effect of multiphoton ionization far outweighs the effect of self-focusing.

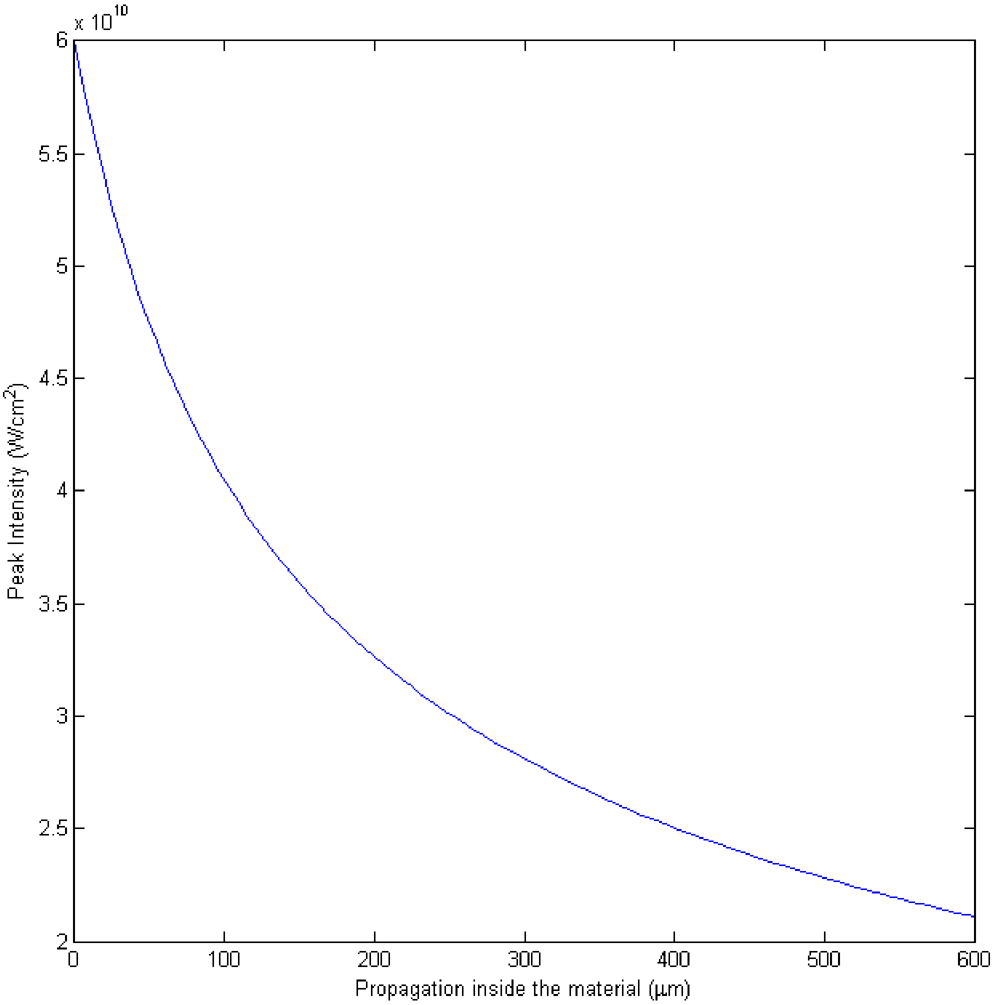

Figure 4.1: Peak intensity of a 1900nm beam undergoing Keldysh ionization as it propagates inside a 600μm GaAs sample. The start peak intensity is 6×10^{10} W/cm^2.

In a similar manner, a soft focusing experiment is developed for the 3100nm experiments. Not only due to self focusing considerations, but by necessity due to the low energy output of the 3100nm laser system. Using a focal length lens of 10cm, we find the beam waist to be 150μm (1/e in field; 250μm FWHM) using a NanoScan system. The Rayleigh range is 2.2cm, leading to a nearly constant beam spot size inside the sample. The critical power (13kW for 3100nm) is breached by the 70MW power for maximum peak intensity. The self focusing distance is 1 mm which is already above the width of the sample. By taking into account the strong multiphoton ionization and using the same argument as above, we show that self focusing is of little effect in the 3100nm experiments.

For both the 1900nm and 3100nm setups, self-focusing will have minimal effect in transmission. In addition, the nonlinear index, n_2, is constant for all polarization directions normal to the propagation direction along the [100] axis in GaAs. Therefore, there can be absolutely no difference in transmission along changing direction of laser polarization.

We conclude that self-focusing, although present, will have little effect in the experiments. We still run the risk of filamentation, where small perturbations in the beam may cause micro-self focusing. To completely model this processes, Maxwell's equations need to be solved together with an ionization model, which is outside the scope of this thesis.

4.1.3 Phase Advance

Phase advance may occur when the refractive index is decreased due to plasma creation in the material. Due to the pulse spatial intensity profile, the beam will diverge (or self-defocus). Plasma is created through the ionization process. We estimate the effect that phase advance may have in our experiments.

From the classical electron oscillator model (Drude model for dielectrics and semiconductors), the relative dielectric constant, ϵ, for the case of an electron plasma is given by,

$$\epsilon(\omega) = 1 - \frac{N}{N_{cr}(\omega)} \tag{4.7}$$

where N is the free electron (plasma) density [cm^{-3}], and $N_{cr} = \epsilon_0 m\omega^2/e^2$ is the critical plasma density [cm^{-3}] (3.1×10^{20}cm^{-3} for 1900nm), and m is the effective mass. Using $\Delta\epsilon = 2n\Delta n$ along with eqn.(4.7), the change in refractive index due to plasma creation is [3],

$$\Delta n(\lambda) = -\frac{e^2\lambda^2\Delta N}{8\pi^2 n_0\epsilon_0 c^2 m} \tag{4.8}$$

As the material is ionized by an incoming electric field, the carrier density will increase, reducing the refractive index. With a laser beam having a Gaussian-type profile, the decrease in index will be greatest at the peak and will lessen toward the wings. This creates a negative lens inside the material, causing the phase front to be advanced and the incoming beam to diverge.

Since the beam waist is constant for soft focusing and the Rayleigh range is larger than the sample thickness, the change in index can be considered constant over the sample thickness. In order to find when the divergence becomes significant, the phase advance, ϕ_c, is estimated,

$$\begin{aligned} \phi_c &= \int \frac{2\pi\Delta n_0 dz}{\lambda} \\ &= \frac{2\pi\Delta n L}{\lambda} \end{aligned} \tag{4.9}$$

To find the minimum carrier density, N, to achieve significant phase advance , we set $\phi_c = \pi$. By rearranging, we find that $\Delta n = \lambda/2L$. By substituting into eqn.(4.8), we find that the necessary carrier density is,

$$N_\pi = \frac{2\pi n\epsilon_0 c^2 m}{e^2 w_0^2} \tag{4.10}$$

where we have given the subscript π to represent the ionized electron density necessary to reach a phase advance of π. For GaAs, $N_\pi = 9.66 \times 10^{15}$ cm^{-3} and 1.74×10^{15}cm^{-3} for the 1900nm and 3100nm experiments respectively.

For an input Gaussian beam, the input laser fluence is given by $\sim I\tau_{FWHM}$. Using the maximum peak intensity in GaAs of 6×10^{10} W/cm^2 , we get an input fluence of $\sim 0.0045 J/cm^2$ for both experiments. The fluence removed from the beam through ionization to reach a phase advance of π is $\sim N_\pi E_g L$ assuming a constant interaction region over the full length of the sample, such that L= 600μm. We estimate the minimum transmission for which the phase advance becomes significant by taking the ratio of remaining fluence in the beam over the input laser fluence. We find that for the 1900nm experiments, the minimum transmission is 0.56. Using our Keldysh model, we find that this value of transmission is not reached until peak intensities are greater than 14×10^{10} W/cm^2, which is not possible in our experiments. In the Results section, we will show that the lowest transmission achieved in the 1900nm experiments is ~ 0.75.

Thus we can be certain that there will be negligible effect from phase advance in the soft-focusing experiments.

4.2 1900nm Experiments

The 1900nm experiments were performed at the Steacie Institute for Molecular Sciences (SIMS) at the National Research Council Canada (NRC) in Ottawa, Canada. In this section, we outline the 1900nm experimental setup including properties of integral components.

The 1900nm is created using the idler of a Light Conversion fs-TOPAS optical parametric amplifier (OPA). This is a superfluorescence seeded OPA that undergoes type II phase matching, meaning that the polarizations of the two output beams are perpendicular to each other.

4.2.1 Optical Parametric Amplifier

The OPA works on the nonlinear $\chi^{(2)}$ process of difference frequency generation (DFG). The pump beam (ω_3) is converted into a signal beam (ω_1) and idler beam (ω_2) according to the equation;

$$\omega_3 = \omega_1 + \omega_2 \tag{4.11}$$

The external alignment into the OPA is given in Fig.4.2. The regen compressor is the final component of the regen laser system. Symbols P and M represent pinholes and mirrors respectively. For day-to-day alignment, the output of the pump laser is set to the chosen energy of 800μJ and aligned through P1. Mirrors M1 and M2 are used to align the beam through pinholes P2 and P3 respectively. The central yellow box defines the optics of the telescope which compensates for any changes in the divergence of the regen output beam. When the beam is aligned through all pinholes, the telescope is well-aligned. M3 is used for fine alignment into the OPA, on a daily basis. The OPA is fs-TOPAS from Light Conversion.

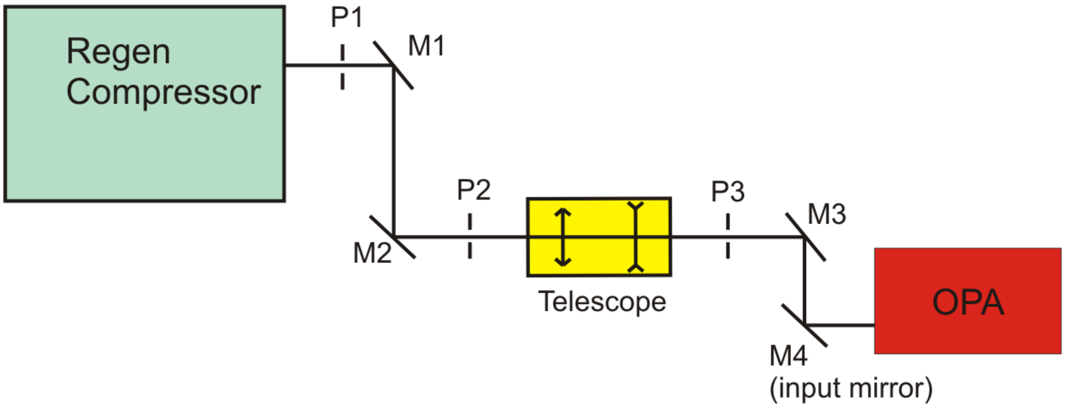

Figure 4.2: External alignment into the OPA. Components P and M are pinholes and mirrors respectively.

Inside the TOPAS, the 800nm pump beam enters and is split into three stages using two beam splitters. In the first stage, the pump (800nm) is sent though a BBO nonlinear crystal and creates superfluorescence. The superfluorescence overlaps with the beam from second stage (preamplifier beam, 800nm) in the same BBO crystal, where it undergoes DFG to create the OPA seed. The BBO Crystal is set to a specific angle, so that the desired frequency is phase matched. The seed is a weak beam containing both the signal and idler outputs from the DFG. The seed is then overlapped again in space and time in the crystal with the beam from the third stage (amplifier beam, 800nm) to amplify the seed to create the final signal and idler beam outputs. With the TOPAS, the signal can be varied from 1200nm to 1600nm. The signal wavelength is measured by sending the beam through a BBO crystal to an Ocean Optics spectrometer, whose maximum wavelength input is 1000nm. The idler wavelength is determined by using eqn.(4.11).

For these sets of experiments, the pump beam comes from a regeneratively amplified Titanium Sapphire laser which outputs 800nm, 50fs pulses at 500Hz and 800μJ per pulse. The output idler beam has a centre wavelength of 1900nm, which corresponds to a photon energy of 0.6eV per photon. For GaAs, this corresponds to 3-photon absorption. The full width half maximum (FWHM) pulse duration is 75fs. The idler has a repetition rate of 500Hz and a pulse energy that we varied from 0.9μJ to 6μJ. The experimental parameters are summarized in Table 4.1. The polarization state of the output is tested using a Glan-Taylor polarizer (Thorlabs GT10) and is shown in Fig.4.3. The idler beam is sent through the polarizer and the transmitted signal is collected with a Thorlabs DET10D InGaAs photodiode. The polarizer is rotated over 200° and the resulting photodiode signal is plotted. The

Table 4.1: Laser and Experimental Parameters

	1900nm	3100nm
Pulse Duration (fs FWHM)	75	92
Repetition Rate (Hz)	500	100 x10^3
Maximum pulse energy (μJ)	6.0	1.6
Beam radius before focus (mm)	1.1	4.0
Lens Focal length (mm)	200 (soft focusing)	100
N-photon Absorption	3	4

curve is fit with a $\cos^2(\alpha+\delta)$ function, where α is the polarizer angle and δ is some phase shift. The contrast ratio between the minimum and maximum values of the function is 1:80.

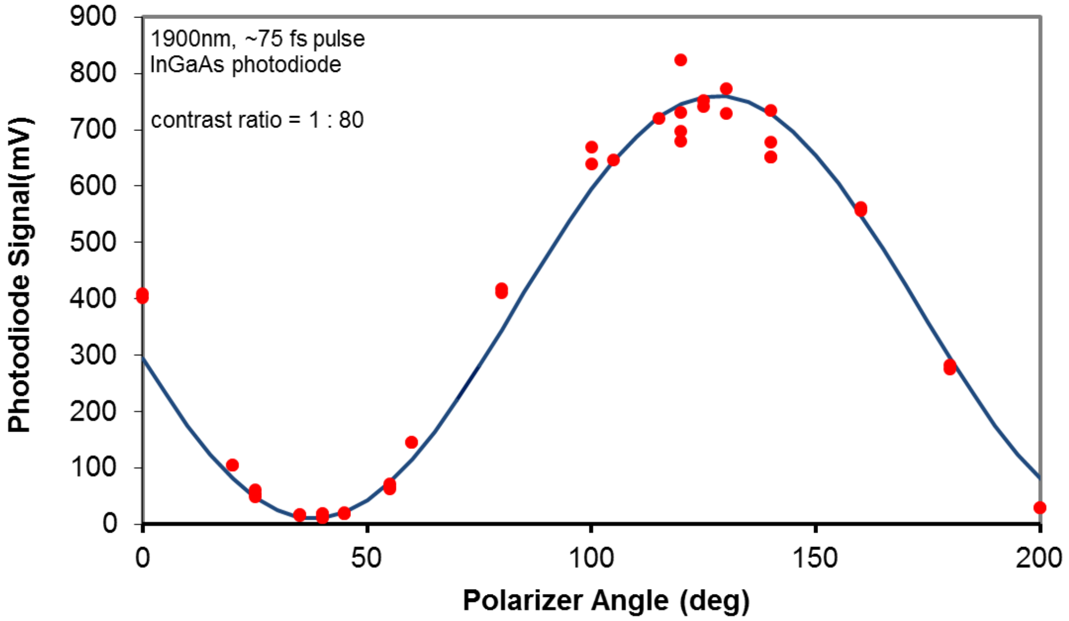

Figure 4.3: Polarization state of the TOPAS 1900nm idler. The contrast ratio is determined using a Glan-Taylor polarizer and InGaAs photodiode.

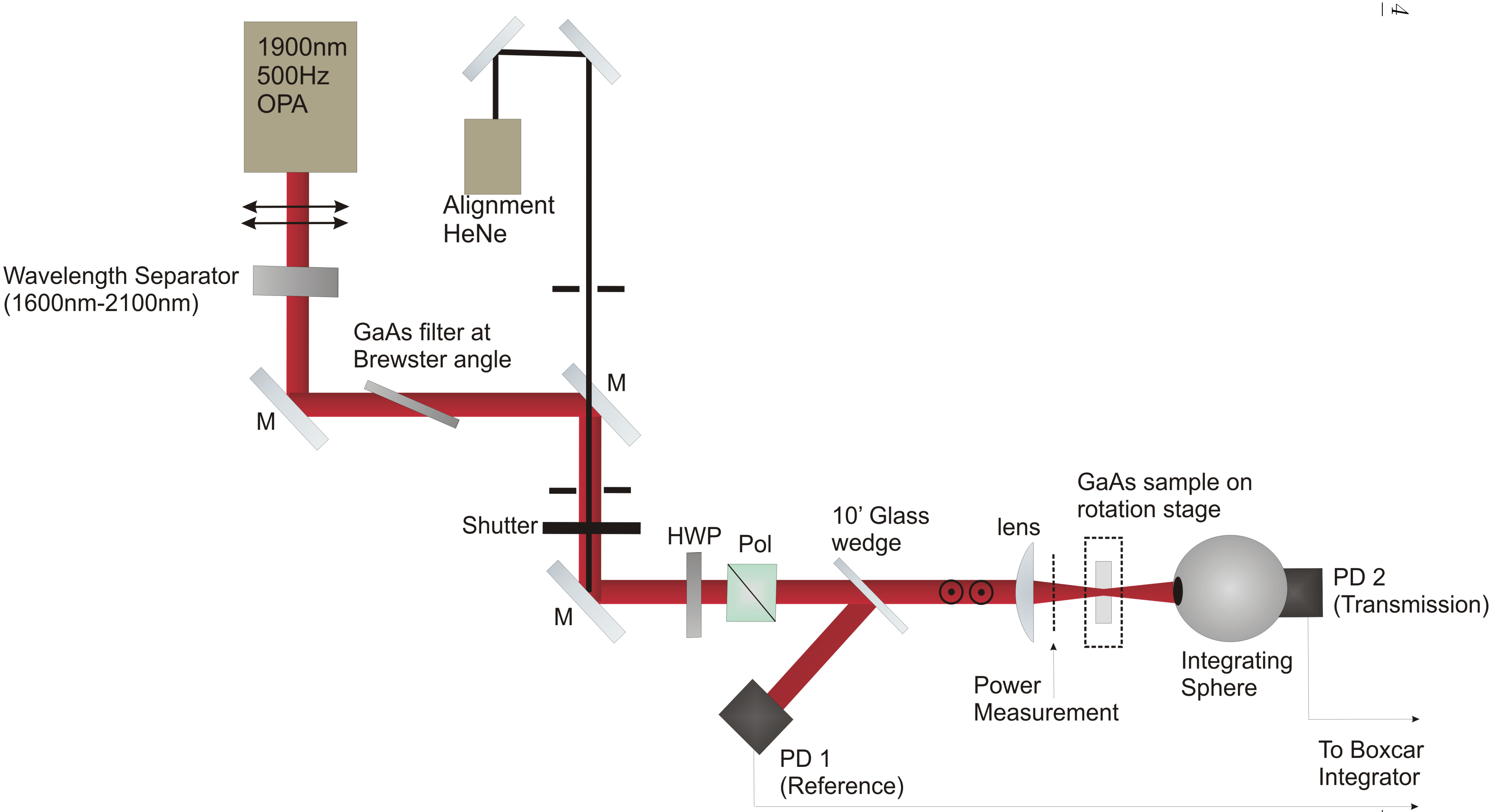

Figure 4.4: Schematic of the mid-IR experimental setup

4.2.2 1900nm Setup

The schematic setup for the 1900nm experiments is shown in Fig.4.4. This setup starts with the idler output of the OPA. The idler is first sent through a series of wavelength filters. A two-dielectric mirror filter (Light Conversion WS11, s-polarized) separates the signal and idler beams, and a 600μm GaAs crystal set at the Brewster angle (73°) filters out any residual wavelengths that may have been created through additional nonlinear processes occurring within the OPA.

An alignment helium neon (HeNe) laser is used for alignment purposes since the idler beam is extremely weak and difficult to detect and align.

The idler beam passes through a shutter (Uniblitz T132) which guarantees the exact same number of shots to hit each angle of the crystal, when rotated.

A half waveplate (HWP, Thorlabs 1200-1650nm) and polarizer (LPNIR100-MP) are automated to control the input energy of the idler beam. The energy is determined using a reference photodiode (PD1). A calibration is made to relate the reference photodiode to the power measurement (Gentec TPM-300) taken at the dotted line (directly before the sample, seen in Fig.4.4). The beam radius directly before the focusing lens is 1.1mm, as measured with a knife-edge (See Appendix D). The beam is sent through a plano-convex lens to focus into the sample. The power loss through the lens is taken into account in the power calibration. The lens is mounted onto a manual translation stage. Two sets of experiments are performed using two different focal lengths; 35mm and 200mm for hard and soft focusing respectively. This is the only difference between the two experimental setups.

The sample is mounted by hand onto a kinematic mount on an automated rotation stage (Newport PR50CC). This stage is mounted onto two independent linear translation stages (Newport VP-25XA and ILS100CC) which allow for full three-dimensional control. All automated stages are controlled with the Newport XPS controller. The sample is aligned for normal beam incidence by establishing a stationary HeNe reflection during rotation. The beam is initially vertically polarized when entering the sample. This is defined as 0° sample angle, which corresponds to the [001] axis aligned along the polarization.

The laser transmission through the sample is collected with an integrating sphere (for soft focusing) to account for any divergence changes. The photodiode for both the transmission and reference are Thorlabs InGaAs DET10D.The responsivity of these photodiodes is shown in Fig.4.5. The responsivity increases from 1.2μm and peaks around 2.2μm. For the experiments using 1.9μm, the responsivity is ~ 1

A/W. The photodiode is chosen because this responsivity to 1.9μm allows for modulation in transmission to be seen immediately by eye, without the need for a Fourier transform.

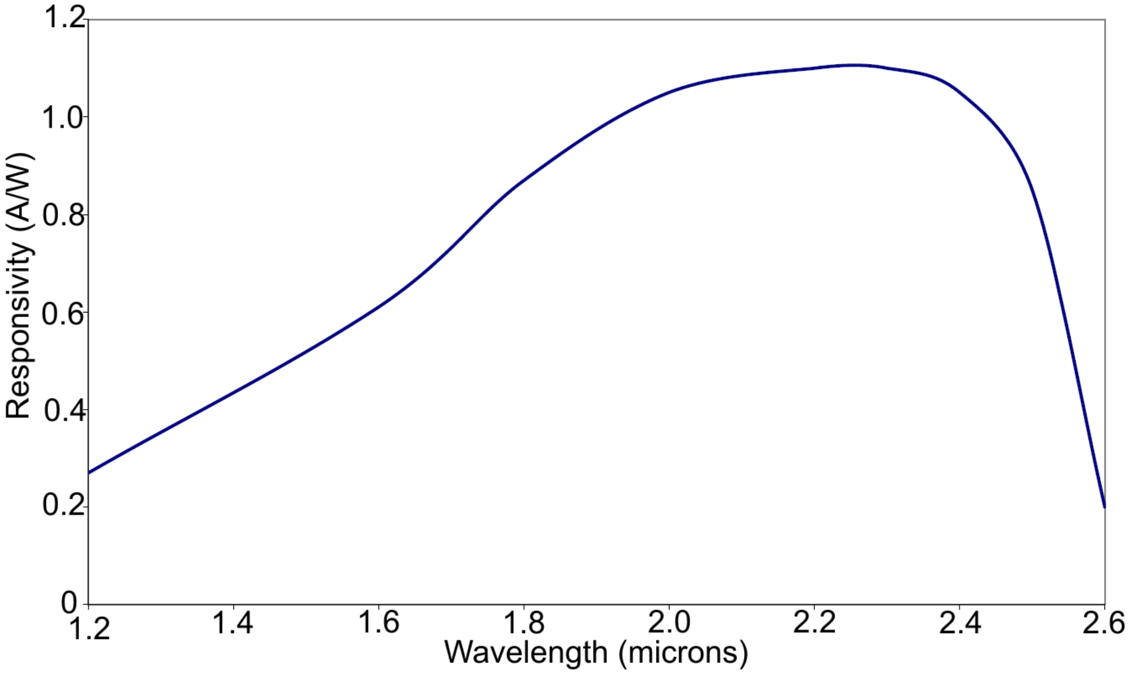

Figure 4.5: Responsivity of the Thorlabs DET10D photodiode.

The power response of the InGaAs photodiodes to the 1900nm signal is given in Fig.4.6. The idler is sent through a half-waveplate and polarizer to vary the beam energy. The power is measured with a powermeter and the signal from the photodiode is sent to an oscilloscope to read off the peak value. The signal increases linearly and begins to saturate after $\sim$ 1000mV. All experiments are performed to keep the signal below 800μJ, to avoid nonlinear response.

The response time of the photodiode is 25ns which is too fast to be gathered by the data acquisition card (DAQ) used, so the signal must first be sent through a boxcar integrator. The boxcar integrator averages the signal and elongates it from 50ns to 10μs. An SRS pulse generator creates the reset trigger for the boxcar. The gate window from each boxcar is set to grab the PD pulses. The sensitivity of each boxcar is set to create a peak output signal with an amplitude similar to input pulse. The response of the boxcar integrator is not linear. However, the photodiode power calibration are taken after the boxcar integrator and take into account all non-linear behaviour. The boxcar output is sent to the DAQ card, which has a sampling rate

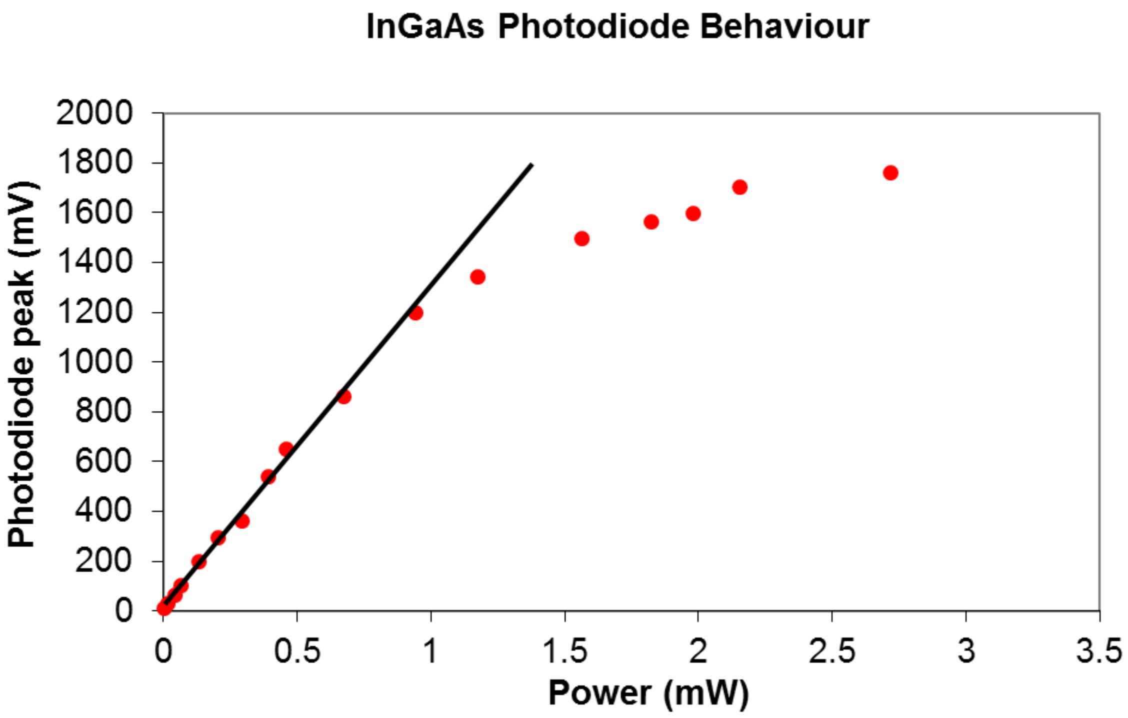

Figure 4.6: Power response of InGaAs DET10D photodiode to a 1900nm laser with no filtering.

of 0.5MS/s for each of the two PD channels. The DAQ performs a single grab of the boxcar output pulses within the time window of the open shutter. This allows for shot-to-shot measurements for both the reference and transmission signals. Each frame of pulses is saved in a separate .txt file, along with all parameters, including the stage positions and length of grab window.

4.3 3100nm Experiments

These experiments were performed at the Institute for Photonic Sciences (Institut de Ciences Fotoniques: ICFO) in Castelldefels, Spain. In this section, we discuss the OPCPA laser setup which creates the 3100nm beam. This is the preliminary setup for the system. We discuss technical properties of the laser output and necessary improvements to the setup.

4.3.1 OPCPA laser system

The 3100nm laser system is based on optical parametric chirped pulse amplification (OPCPA) as fully described in [7]. The laser consists of a three-stage amplified system as shown in Fig.4.7. A seed pulse is generated by difference frequency generation (DFG) in a 2 mm long PPLN crystal using 1.07 μm and 1.58 μm outputs from a Toptica fibre laser oscillator running at 100 kHz. The first and second stages consist of an OPA; the first of which uses a 2 mm long PPLN crystal to amplify the DFG seed pulse by pumping with an 8 ps Lumenera laser operating at 100 kHz. The third stage OPA uses a 1.4 mm PPLN crystal to further amplify the beam.

The output laser has a spectrum centred at 3.1 μm as shown in Fig.4.8, with a FWHM duration of 92 fs. The repetition rate is 100 kHz, with a $1/e^2$ intensity beam radius before focusing of 4 mm. The pulse energy ranges from 0.2μJ to 1.6μJ.

At 3100nm the pulse energy can not be varied using the traditional half-waveplate polarizer method due to lack of an achromatic waveplate. The laser energy is tuned by delaying the pump pulse (D4) delivered to the third amplifier stage (OPA_3 in Fig. 4.7). By changing the temporal overlap of the pump pulse with the chirped seed pulse, the efficiency of amplification is modified to allow for a range of possible output energies. The output spectrum of the OPCPA laser is shown in Fig.4.8. The various curves represent the normalized spectra for changing delays of the pump and seed pulse in the final amplification stage. The blue spectrum occurs at maximum power when the pump and seed are overlapped. The seed pulse is chirped, so any delay in the pump-seed temporal overlap will result in greater amplification of the red or blue portion of the OPCPA spectrum. We show the effects on the spectrum by delaying the overlap in opposite directions. The green spectrum in Fig.4.8 occurs when the pump is delayed with respect to the seed to amplify more of the red portion of the seed. The red spectrum occurs when the pump is delayed with respect to the seed to amplify more of the blue portion. The red spectrum is nearly identical to

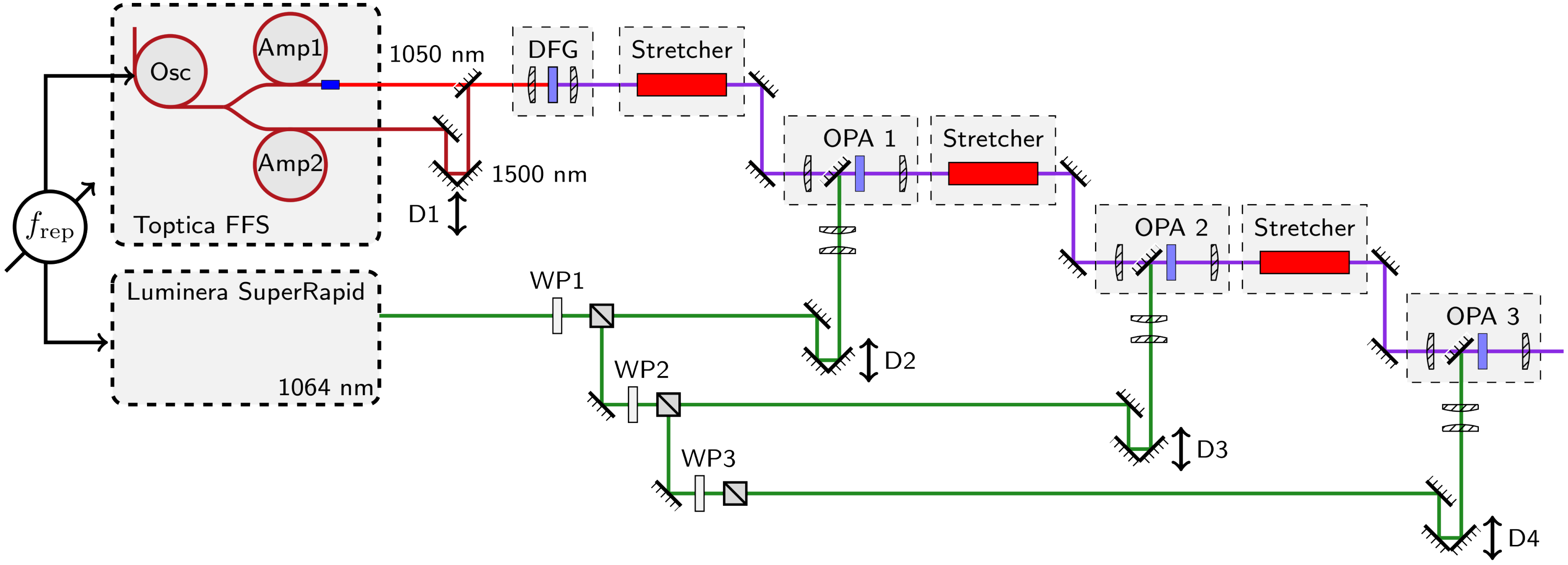

Figure 4.7: Schematic of the mid-IR laser OPCPA system [7].

the spectrum at maximum power. However, the green spectrum appears to be asymmetric and have have a greater magnitude toward the longer wavelengths. Thus when adjusting the energy, we delay the pump toward the blue portion to the seed pulse.

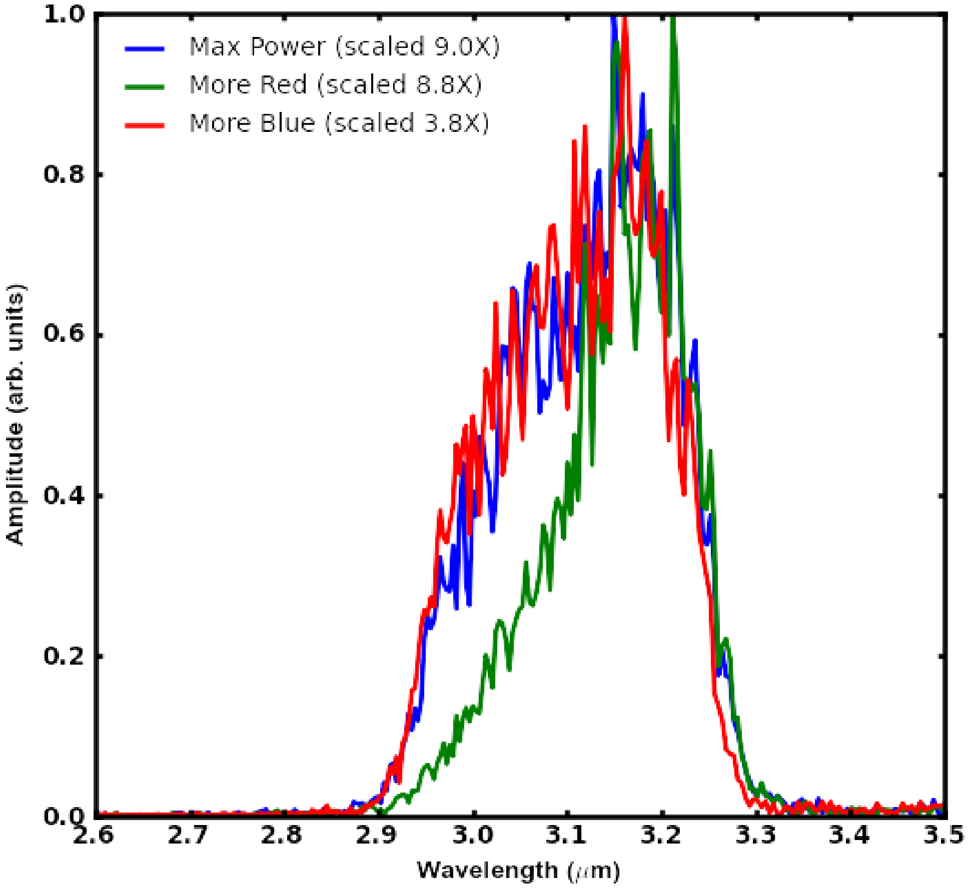

Figure 4.8: Spectra of the OPCPA Laser for different translation stage delay settings. The blue line shows the optimized output, the green curve shows the spectrum if the blue end of the chirped seed is clipped in the gain curve when translating the stage. The red curve shows the output spectrum when the red side of the chirped seed is clipped when translating the stage.

The transmission is detected with a Thorlabs DET10D photodiode (PD), whose response is given in Fig.4.5. The photodiodes are more sensitive to the blue end of the spectrum (the responsivity dropped from 1.0 A/W to 0.2 A/W from 2.4 μm to 2.6 μm, as seen in Fig.4.5). The detector responsivity can not be found up to a wavelength of 3100nm. These detectors allow for preliminary detection of a modulated transmission with the 3100nm, but will not be used for complete characterization of this nonlinear effect using 3100nm.

4.3.1.1 Amplified Spontaneous Emission

When experiments were first performed, there was concern over the magnitude of the laser intensity inside the sample. The amplified spontaneous emission (ASE) was examined to rule out residual energy in the pulse which may not contribute to ionization.

In a traditional laser cavity amplifier, energy is stored in the laser crystal in a population inversion and the energy is extracted when it is stimulated by a seed pulse. However, photons may spontaneously decay from the crystal and then consequently get amplified in a process known as ASE [19]. This may create a energy pedestal on the outgoing pulse and as a result lead to a lower peak intensity than expected for a given pulse energy.

In the OPCPA system, the energy of the DFG pulse is amplified by via a parametric process. There is nearly pure energy conservation between the pump and the amplified output, since the process involves excitation to a virtual level in the crystal. To prove that no energy is being lost to ASE, the following variations in the setup were tested and compared to the total amount of energy delivered to the output when all three OPA parts were pumped with the full pump power:

1. delayed the 1550 nm output from the 1050 nm pulse to prevent DFG
2. blocked the 1550 nm
3. blocked the 1050 nm
4. adjusted the phase delay between the two laser systems such that the seed and pump pulses did not overlap in time in the crystals

For all tests, the output power dropped more than 4 orders of magnitude; lower than the noise from the detector. Thus we can confirm that there is negligible ASE in the laser system.

4.3.1.2 Dispersion

To focus into the GaAs sample, a CaF_2 lens is used (see Fig.4.9). Another concern with the laser system was the dispersion that may be caused by the CaF_2 lens. The pulse width of the focal point, neglecting chromatic aberrations by the lens, could be stretched by the group velocity dispersion (GVD) of the CaF_2 lenses and optics used in the experiment. The group velocity dispersion (GVD) is calculated as:

$$GVD = \frac{-\lambda^3}{2\pi c^2}\frac{d^2 n}{d\lambda^2} \qquad (fs^2/\mu m) \tag{4.12}$$

where $\lambda = 3.1$ μm is the centre wavelength, and n is the index of refraction of CaF_2, calculated using the Sellmeier coefficients. With the same coefficients, the second derivative with respect to wavelength is -2.268×10^{-3} μm^{-2}, giving a GVD of -0.1070 $fs^2/\mu m$.

From the Melles-Griot catalogue [2], the final FWHM pulse width, τ_1, of an assumed FWHM transform-limited pulse input, τ, can be estimated as:

$$\tau_1 = \tau * \sqrt{1 + \left(\frac{4\ln 2 \times d \times GVD}{\tau^2}\right)^2} \tag{4.13}$$

For an input pulse width of 92 fs as stated above, the output pulse from a 5 mm thick CaF_2 optic would be 93 fs. So the optics will not contribute to significant pulse dispersion.

4.3.2 3100nm Setup

After the OPCPA system output, the beam is directed into the external setup shown in Fig.4.9. A reference beam is picked off the laser output beam using a wedge and photodiode (Thorlabs DET10D). The reference is used together with a power calibration (Fig.4.9) to determine the energy at the sample. The beam is sent through a CaF_2 lens which is mounted to a manual linear translation stage. The experiments were done using a 10 cm antireflection (AR) coated lens. The sample is mounted onto a kinematic mount which is then mounted to a automated rotation stage (Newport PR50CC). This stage is mounted onto two independent linear translation stages (Newport VP-25XA and ILS100CC) which allow for full three-dimensional control. All automated stages are controlled with a Newport XPS controller.

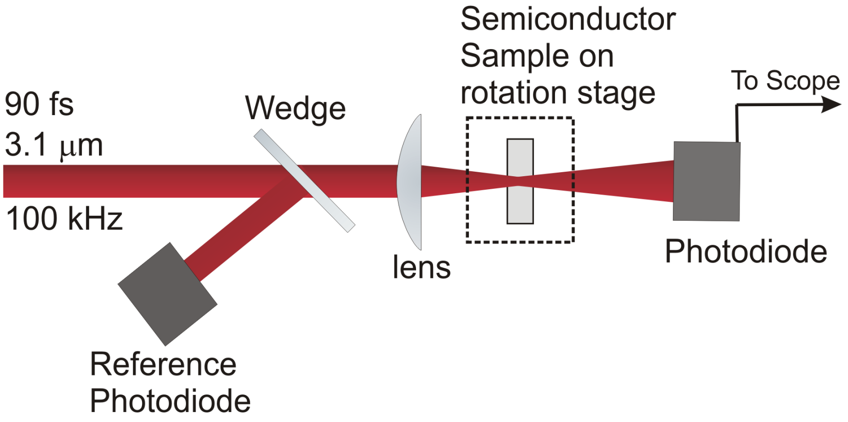

Figure 4.9: Optical setup to measure transmission modulation.

The transmission is detected by an unfiltered DET10D photodiode. The aperture of the photodiode was 1.0 mm in diameter. So to minimize the detector sensitivity to pointing changes, a divergent lens was placed a few centimetres from the photodetector to expand the beam. This lens was necessary since ground glass or scotch tape (as a scattering material) degraded the signal to below detectable levels. An integrating sphere could not be used due to the low energy output of the laser. The pulse-to-pulse fluctuations were significant ($> 15\%$) and despite averaging, the results are noisy. Since the responsivity of the photodiodes was low (Fig.4.5), the signal level on the photodiodes was low. An amplifier was tentatively connected to the photodiode, but the noise of the amplification made the signal unreadable, and hence could not be used.

The signal from the photodetectors is sent through an oscilloscope, which is saved into a .txt file from an Ethernet cable.

Chapter 5

Results

The ionization (band-to-band transition) of a solid leads to depletion of an ultrafast laser beam. The depletion can be measured in the transmission of the laser through the sample. Through the transmission, we indirectly measure probability of ionization. In this chapter, we highlight the transmission results for both the 1900nm and 3100nm experiments. First, we describe how the raw experimental data is analyzed to retrieve the transmission data. Second, we discuss the appearance of a distinct modulation in transmission for both wavelengths, revealing the symmetry of the GaAs sample. We then show that the trends in transmission and modulation depth can be directly described through Keldysh theory, as described in chapter 3.

5.1 Power Calibrations

To determine the laser power inside the sample for all experiments, we initially calibrate the power of the laser to the reference photodiode signal which is gathered from a laser pick-off before the sample. Using the calibration, we have direct knowledge of the laser power inside the sample at all times during the experiment. The photodiode signal captures a series of pulses, giving information on pulse-to-pulse fluctuations during the course of the experiment.

First we describe how the laser power calibrations are performed for the 1900nm experiments. The incident laser power is measured with a powermeter, directly before the sample The photodiode pick-off reference signal is collected by an unamplified InGaAs peak photodiode, which is identical to the photodiode used for transmission collection. Any pointing error into the reference photodiode is minimized by using a 600 and 1500 grit diffusers placed 2cm from the detector head.

Additional ND filters are used as necessary to keep the maximum signal below the saturation voltage for the photodiode. During the calibration, the power meter blocks the sample, removing all risk of back reflection off the sample. To calibrate the power, the laser output energy is varied using a half-waveplate and polarizer and both the reference photodiode signal and power meter measurements are taken simultaneously. The photodiode collects 50 pulses and the signal is sent through a boxcar integrator to elongate the pulses in time. The average peak photodiode value is calculated. The reference data is treated with the identical method as for the transmission data. A detailed description of the analysis algorithm is given below in section 5.2. From the calibration, the laser power can be determined by comparing subsequent reference photodiode measurements to the given calibration curve. A new calibration is created for every laser alignment through the setup. To find the laser energy inside, we then take into account the reflection off the sample surfaces.

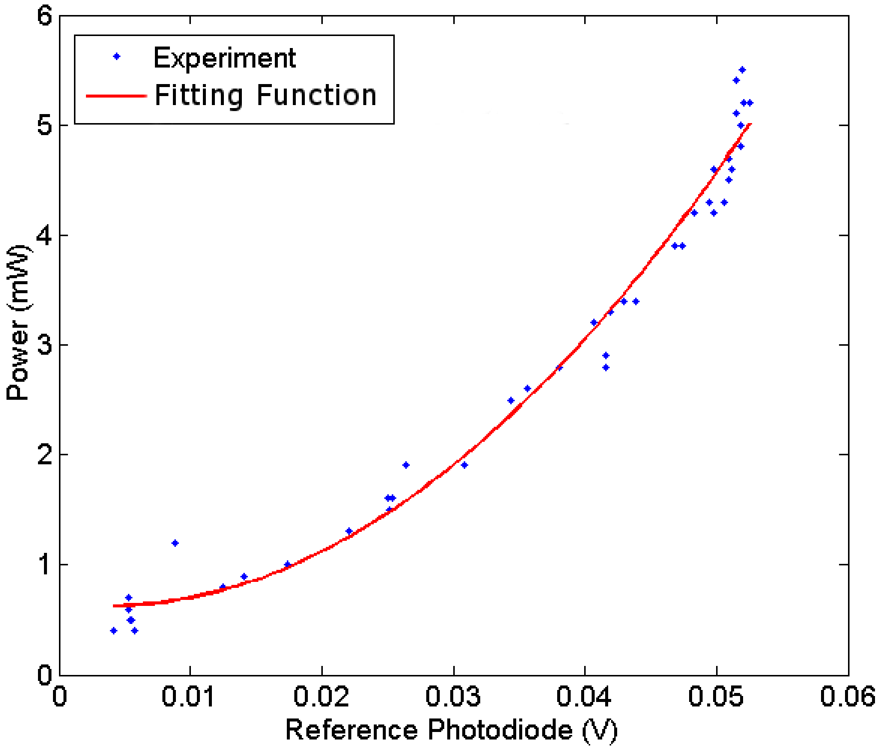

Figure 5.1: Power calibration of the 1900nm system, used for soft-focusing data acquisition. The average peak voltage of the reference photodiode pick-off is plotted in the azimuthal axis. The laser power measured directly before the sample is plotted on the ordinate axis. The red curve is a parabolic fitting function, where P and x represent the average peak power and photodiode signal respectively. The function is given by P(mW)= $1831x^2 - 13.24x + 0.6500$.

For the 1900nm OPA system, the power calibration is shown in Fig.5.1. The calibration data is fit with a parabolic curve, $P = (1.83 \times 10^3 \text{ mW/V}^2)\ x^2 - (13.2\text{mW/V})\ x + (0.650\text{mW})$, where P is the power in mW as measured with a powermeter, and x is the ordinate axis describing the average reference photodiode signal in volts. The non-linear nature of the curve is due to the boxcar nonlinear response. We know this, because experimental measurements of the direct relationship between the powermeter and the reference photodiode signals is linear.

The power calibration for the 3100nm is created by plotting the signal from a photodiode pick-off reference to the laser power as measured with a powermeter. This is similar to that done for the 1900nm laser system. The reference photodiode signal is read from an oscilloscope. Ten pulses are captured for each power and the average of the pulse peaks is calculated. The lens is AR coated and does not affect the power reading. Fig. 5.2 shows the resulting curve. The black dots are the experimental data of the average peak photodiode signal in mV as a function of the laser power in mW. The data are fit with a linear regression with the following parameters: $y = (1.28 \times 10^{-3}\ \mathrm{V/W})\ x - (1.56x10^{-2}\mathrm{mV})$, where y and x represent the photodiode in mV and the power in mW respectively. The errorbars represent the pulse-to-pulse fluctuations present in the photodiode pulse sets used to create the data points.

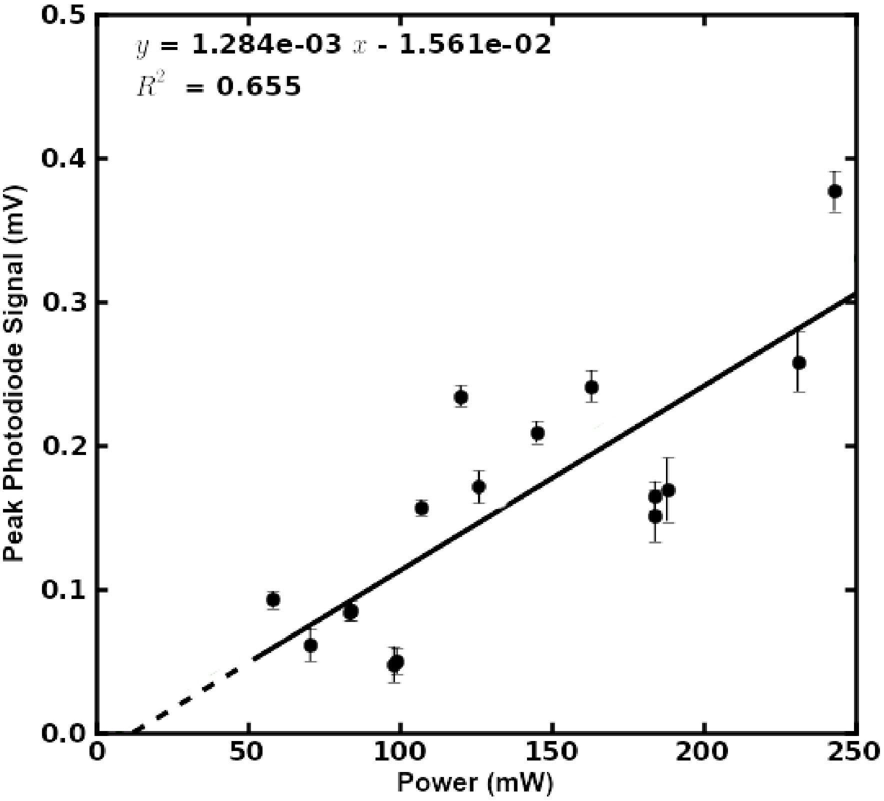

Figure 5.2: Average peak voltage of the reference photodiode directly from the scope measured with respect to the 3100nm OPCPA laser pulse power. The black points are the experimental data. The data is fit with a linear regression with a squared correlation coefficient given by R^2.

5.2 Analysis

Below we describe how the raw data is analyzed for both 1900nm and 3100nm experiments, including power calibrations. The analysis procedure is given as;

1. For every file (sample angle), the pulse peaks are detected above a noise threshold. Both the reference photodiode and transmission photodiode are treated independently.

2. The data points between the peaks (plus pulse width) are averaged, to estimate the noise baseline. The baseline is subtracted from the entire data file.

3. The ratio of each transmission peak is taken over each reference photodiode peak, accommodating for pulse-to-pulse fluctuations.

4. The peak ratios are averaged for each sample file (angle).

5. The energy is determined by comparing the average reference photodiode peak to the energy calibration.

6. Repeat the above procedure for no sample present.

7. Find the transmission by taking the ratio of the transmission signal with sample over transmission without sample, taking into account sample reflection, as in eqn. (5.6).

5.3 Transmission of 1900nm

Our main concern is the electric field - sample angle dependence of laser absorption as measured by beam depletion. First, we show how we will obtain the field intensity inside the sample, given the external pulse energy. We do this by observing the laser transmission as a function of energy. We will experimentally show that the soft-focusing condition is preferred by comparing the transmission curves for both the soft and hard focusing cases. We will show distinct four-fold modulation in transmission as a function of laser polarization in GaAs. We will then use the soft-focusing results in GaAs to show that modulation occurs primarily from ionization of the heavy hole valence band.

To determine the transmission from the data retrieved from experiment, it is necessary to first clearly define transmission. We start with a stationary GaAs sample and direct the laser propagation direction along the [100] axis. Hold the laser polarization stationary along the [001] axis which we will label 0°. For a given input laser energy, the transmission, T, is defined as,

$$\begin{aligned} T &= \frac{E_{out}}{E_{in}} = \frac{E_{in} - E_{abs}}{E_{in}} && (5.1) \\ dE_{abs} &= E_g \; w(I) N dt && (5.2) \end{aligned}$$

where E_g, N, and $w(I)$ are the bandgap, electron number density and intensity-dependent ionization rate respectively, and E_{abs}, E_{in}, and E_{out} are the energy absorbed, input pulse energy, and output pulse energy respectively. The transmission appears to depend both on the energy and intensity of the laser pulse. The intensity and energy are directly related and we have verified with Keldysh theory that the theoretical transmission for an input pulse of a given duration and intensity, is independent of the laser spot size, and is only an expression of laser intensity.

To find intensity inside the sample, we use the power calibrations as discussed above, to get the laser power. The laser pulse energy is found by taking into account the energy loss due to reflection off the sample surfaces. The reflection coefficient is shown in Table (2.1) and is also found experimentally by measuring the incoming and reflected power at nearly 0° incidence for a very low intensity pulse. The reflected measurement is a summation of multiple reflections off the front and back surfaces. Using only the first two reflections and assuming incoherent reflections, $P_R/P_i = R + R(1-R)^2$ where P_R, P_i, and R are the reflected power, incident power and reflection coefficient respectively. The equation is solved to give a reflection coefficient of 0.23. This is compared to the theoretical value of 0.29, from the Fresnel equations for normal incidence. Seeing the similarity between the two values we chose the theoretical value for all calculations. The energy inside the sample is,

$$E_{in} = P(1-R)/[Rep] \tag{5.3}$$

where P is the laser power from the calibration and [Rep] is the repetition rate of the laser. This is assuming no back surface contribution. From the energy measurements, the peak laser intensity can be estimated using eqn. (E.2), which is valid for a Gaussian pulse. However, a more accurate estimate of the intensity can be done by fitting the experimental transmission to the time-space averaged ionization results of transmission from Keldysh theory (See Appendix E).

To find the output energy, E_{out}, we must know how much signal will be detected by the photodiode located behind the sample when there is no absorption. To guarantee no absorption, we remove the sample completely. We will label this condition as "No Sample". We repeat the photodiode measurements and find the laser energy again through the power calibration. If there is no sample in place, then

$$E_{NS} = P_{NS}/[Rep] \tag{5.4}$$

where E_{NS} and P_{NS} are the laser energy and power for an empty sample holder ("No Sample").

We now relate the energy expressions given above to the experimental photodiode measurements in order to find the transmission in terms of measurable quantities. We take the photodiode signal on the transmission side of the sample with the sample present, labelled PD_S, together with the photodiode signal of the empty sample holder, PD_{NS}. Both powers are found from the reference photodiode and power calibration with the first power reading occurring with the sample in place and the second occurring without the sample in place. Aside from variation in the laser energy output, they should be identical. Using the definition for transmission in eqn. (5.1) and eqns. (5.3, 5.4), we deduce expressions for the energy output, E_{out}.

$$E_{out} = \frac{PD_S}{(1-R)} \frac{E_{NS}}{PD_{NS}} \tag{5.5}$$

Therefore, the total transmission is,

$$T = \frac{1}{(1-R)^2} \frac{PD_S}{PD_{NS}} \frac{P_{NS}}{P} \tag{5.6}$$

We now show the results of transmission with respect to intensity. As explained in chapter 4, section 4.1 two focusing conditions are addressed. Hard focusing refers to a focal condition where the focal region (twice the Rayleigh range) is much smaller than the thickness of the sample. Soft focusing refers to the condition where the beam spot is nearly constant within the full sample thickness. We have previously determined that the hard focusing will potentially suffer from additional nonlinear effects including plasma phase advance. Therefore, we will not fit the hard focusing results to theoretical curves. The results for the hard focusing transmission can be seen in Appendix F.

Below we show in Fig. 5.3 the experimental results for a softly focused, 75fs, 1900nm laser beam. The data points represent the experimental transmission data as a function of laser intensity inside the sample. The solid blue and red dashed curves represent the theoretical curves as created by space-time averaged Keldysh theory for heavy hole and light hole excitation respectively. In these experiments, a focusing lens of 200mm is used. An unfocused beam radius of 1.1mm is measured with a knife-edge (See Appendix D). Using a Gaussian beam approximation, the beam will focus to $\sim 110\mu$m beam spot radius. This corresponds to a Rayleigh range of approximately 2cm, which is much greater than the sample thickness of 600μm. The experimental data spans an intensity range of $\sim 2\times10^{10}$W/cm^2 to $\sim 6\times10^{10}$W/cm^2. The minimum and maximum values are established by the minimum and maximum output energy values of the experimental setup respectively. The minimum does not occur at zero intensity because the waveplate used for energy variation creates a slight ellipticity in the beam polarization, which when sent through a polarizer can not give an exact zero value. Finding an ideal waveplate is difficult for a 1900nm laser wavelength. The experimental transmission decreases as the laser pulse intensity increases. This is due to the depletion in the laser beam as a result of absorption of laser energy required for carrier band-to-band transitions. The steep decline in transmission as a function of intensity shows evidence of nonlinear absorption behaviour (Since linear absorption would only depend on the sample thickness and not the pulse energy). The hump seen in the experimental data at $\sim 5\times10^{10}$W/cm^2 is not repeatable. The experiments were performed numerous times and this current data set was chosen for completeness.

Fig. 5.3 shows the theoretical curves describing the effects of ionization (band-to-band excitation) on a propagating laser beam. The first theoretical curve (solid blue) in Fig. 5.3 uses the reduced mass between the lowest conduction band and the heavy hole valence band when determining the ionization rate. The second theoretical curve (dashed red) uses the reduced mass between the lowest conduction band and the light hole valence band when determining the ionization rate. The theoretical simulations use the identical laser and sample parameters as used in the experiments. A full description of the theoretical calculations used to create these curves are given in chapter 3. The absorption is zero at an intensity of zero. As the intensity increases, absorption begins to occur after the threshold intensity, which for GaAs is $\sim 1.6 \times 10^{10}$ W/cm^2. The transmission slope in Fig.5.3 for 0^+ intensity appears much greater than it actually is due to the small intensity step-

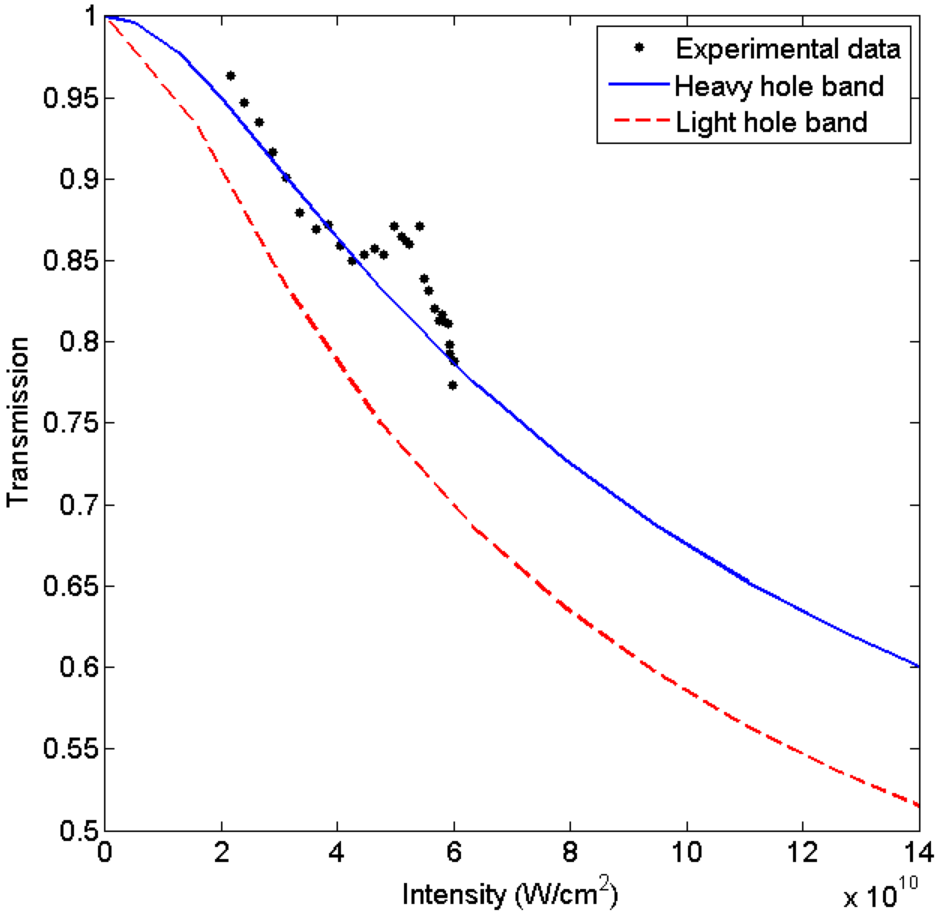

Figure 5.3: Transmission through 600μm (100)GaAs for a softly focused 75fs, 1900nm laser beam. The data markers represent the experimental data, and the solid blue and dashed red lines are the theoretical transmission curves for the heavy and light hole band ionization respectively.

size of theoretical simulations. As seen in Fig.5.3, the experimental transmission lies close to the predicted heavy hole transmission curve. We expect that the carrier ionization should be dominated by the light hole ionization rate. The fitting may appear arbitrary since there is uncertainty in the experimental intensity. However, more importantly our intensity calibration needs to fit with the modulation depth measurements as described in the next section. This is a better experimental fitting parameter in that it more clearly decides between the heavy hole and light hole simulations. In addition, to remind the reader, the modulation of transmission is the primary focus of this thesis.

5.4 Transmission Modulation of 1900nm

In this section, we show direct measurements of the modulated transmission of a 1900nm laser with GaAs sample angle. First we define modulation depth with regards to the experimental results. We use the laser intensity as determined by the transmission curves above to plot the modulation depth with respect to laser intensity. The modulation depth is fit to the simulated curves based on Keldysh theory for both heavy and light holes, as described in chapter 3.

To view the transmission modulation, the sample is rotated in a plane normal to the laser propagation direction, under constant laser polarization. The transmission, T, is found for each angle, θ. To determine modulation depth, the modulation curve is fit with a $\sin^2 k\theta$ curve using the MatLAB least square fit, where θ is the sample angle with respect to laser polarization and $k = 2$ is the fitting parameter found. In reference to the sinusoidal fit;

$$\text{Modulation Depth} = \text{MAX(T)} - \text{MIN(T)} \tag{5.7}$$

where MAX and MIN refer to the maximum and minimum values of the fitting $\sin^2 2\theta$ curve respectively, as visually represented in Fig.5.4.

In all experiments, the laser propagates along the GaAs [100] axis. An angle of 0° corresponds to the laser polarization positioned vertically, along the [001] crystal axis. This position corresponds to the minimum transmission, and hence largest absorption rate.

Fig.5.4 shows the preliminary results for this thesis experiment, which were performed for the hard focusing case. We use this set to define the modulation parameters and discuss these results in depth. The hard focusing data are partial to additional nonlinear effects, as discussed in chapter 4.1 and shown in Appendix F. Thus we will not fit the data to theory. Thorough discussions will focus on the soft focusing condition.

The hard focusing curve is presented here to demonstrate that the modulation is a robust feature regardless of the optical details. Furthermore, the frequency of the modulation with angle remains consistent regardless of experimental conditions.

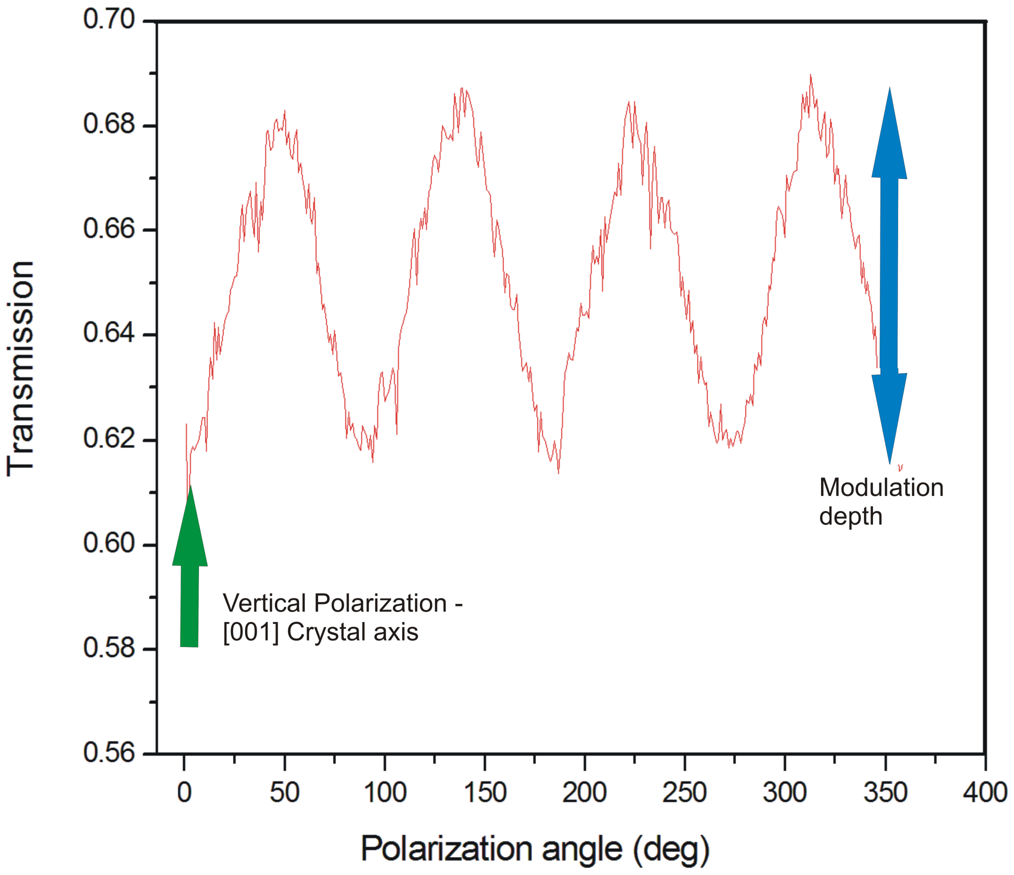

Figure 5.4: Transmission modulation of a tightly focused (focal length = 35mm), 1900nm, 75fs FWHM laser through 600μm (100) GaAs. The 0° corresponds to the [001] axis, as highlighted by the green arrow. The blue arrow highlights the modulation depth.

Deep transmission modulation is seen for all experimental cases, including soft and hard focusing conditions for 1900nm laser transmission. However, we will focus our discussion on the soft focusing data results. We show the results for a softly focused, 1900nm, 75fs laser pulse in Fig.5.5. Experimental parameters can be seen in Table 4.1.

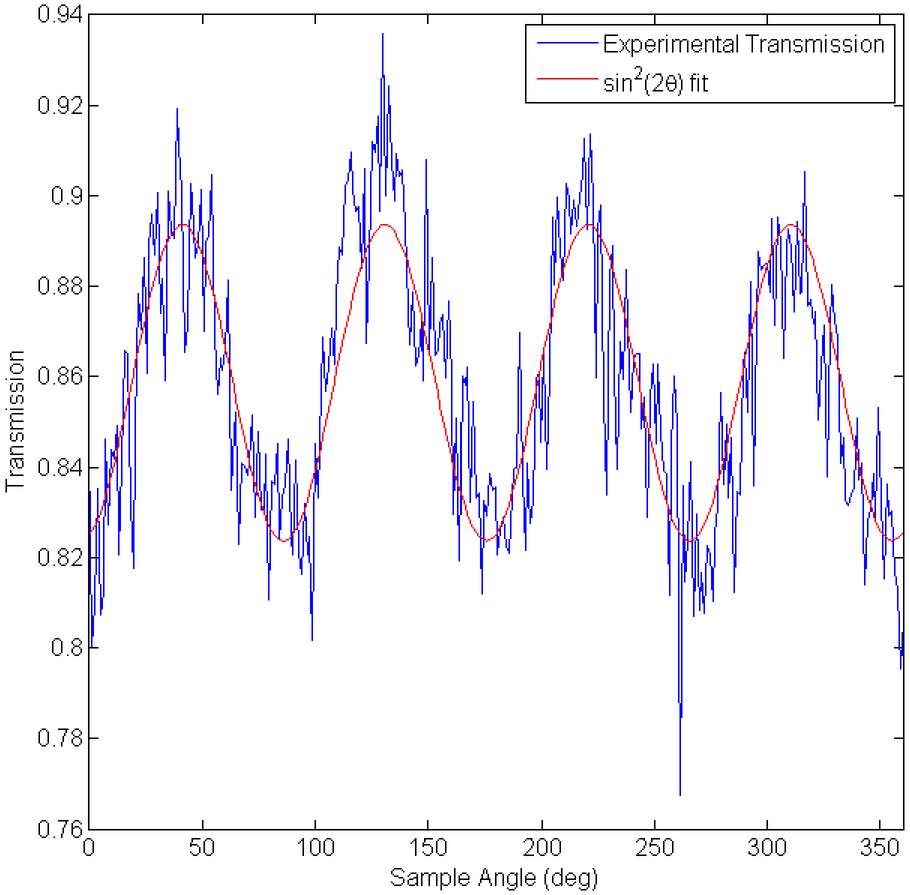

Figure 5.5: Modulation of laser transmission through 600μm (100) GaAs for a softly focused 75fs, 500Hz, 1900nm laser beam. The 0° corresponds to the [001] axis.

This particular plot corresponds to a transmission of $T \approx 0.82$, which has an intensity of ~6x10^{10} W/cm^2. Similar plots are made for all transmission data for varying energy as seen in Fig. 5.3. The data appears more noisy than the plot seen in Fig.5.4, purely due to the pulse-to-pulse fluctuation in the laser source. The experimental data is fit to a $\sin^2(2\theta)$ fitting curve and shown as the smooth red curve. The least square error between the modulation data and the $\sin^2(2\theta)$ fit is almost

2%, which is similar to the pulse-to-pulse fluctuations of the laser. From this fitting curve, we find the period to be 89.7°, which verifies that there is a four-fold symmetry (repeating every 90°), which is expected for the cubic GaAs crystal. Again, this result is persistent regardless of the focusing conditions. From the fitting curve, the modulation depth is found as represented in Fig.5.4. In Fig.5.5, the modulation depth is $\sim 5\%$. For all transmission modulation curves taken in this experimental set, the modulation depth ranges from 2% to 5%. Compare these values to the previous work done by Gertsvolf *et.al* [10], where modulation depths of $\sim 0.4\%$, $\sim 0.2\%$, and $\sim 1\%$ were seen for α-quartz, sapphire, and lithium fluoride respectively, as shown in Fig.1.2. Thus we see significantly larger transmission modulation in GaAs than in the previous dielectrics experiments. This allows us to view the modulation in real-time without the need for Fourier transformations, which was necessary in the previous work.

In Fig.5.5, we see that the minimum transmission and hence maximum absorption occurs at the 0° angle which corresponds to the laser polarization oriented along the [001] axis. Due to symmetry, we get the same transmission every 90°, which correspond to the $[0\bar{1}0]$, $[00\bar{1}]$, and [010] axes for $\theta = 90°, 180°$, and 270° respectively. This sample was rotated over several revolutions and showed no change in modulation, thus revealing no evidence of sample damage.

The GaAs sample is rotated 360° for each increased laser pulse energy and the modulation depth is found for each pulse energy. The pulse energy is found by using the power calibration as described previously. We plot the modulation depth as a function of intensity in Fig. 5.6. The intensity inside the sample is determined by scaling the experimental intensity to the theoretical modulation depth curve as seen in Fig.5.6. The points represent the experimental data and the solid blue and dashed red lines are the theoretical transmission curves for the heavy and light hole band ionization respectively. The large fluctuation seen in the experiment around 0.5×10^{10} W/cm^2 is due mainly to power fluctuations from the laser propagating through the OPA. The theoretical curves show an initial increase in modulation depth as ionization begins to occur in the sample. This is due to the fact that the ionization rate at some angles is larger than other angles. Fig.5.5 shows that there is little ionization at $(2n + 1)\pi/4$ degrees compared to ionization at $n\pi/2$ degrees, where $n \in \mathbb{Z}$. As the intensity continues to increase, the modulation depth plateaus when ionization at $(2n + 1)\pi/4$ degrees is no longer negligible. At much larger intensity, the modulation depth declines as the pulse is depleted of photons, showing less variation between transmission along different sample angles.

The experimental data clearly follows the curve as predicted using Keldysh ionization from the GaAs heavy hole valence band. Although the ionization rate of the light hole valence band is greater than for the heavy holes, as discussed in chapter 3, the heavy hole valence band shows a much greater variation in effective mass as a function of angle. The ionization rate from the heavy hole band varies by 33.7% while the light hole band varies by only 8.7% (Both depths calculated theoretically for a peak intensity of 10×10^{10} W/cm^2 and averaged over the laser spot). Refer to Fig.3.2 for the theoretical ionization rates for the heavy and light hole bands as a function of sample rotation angle.

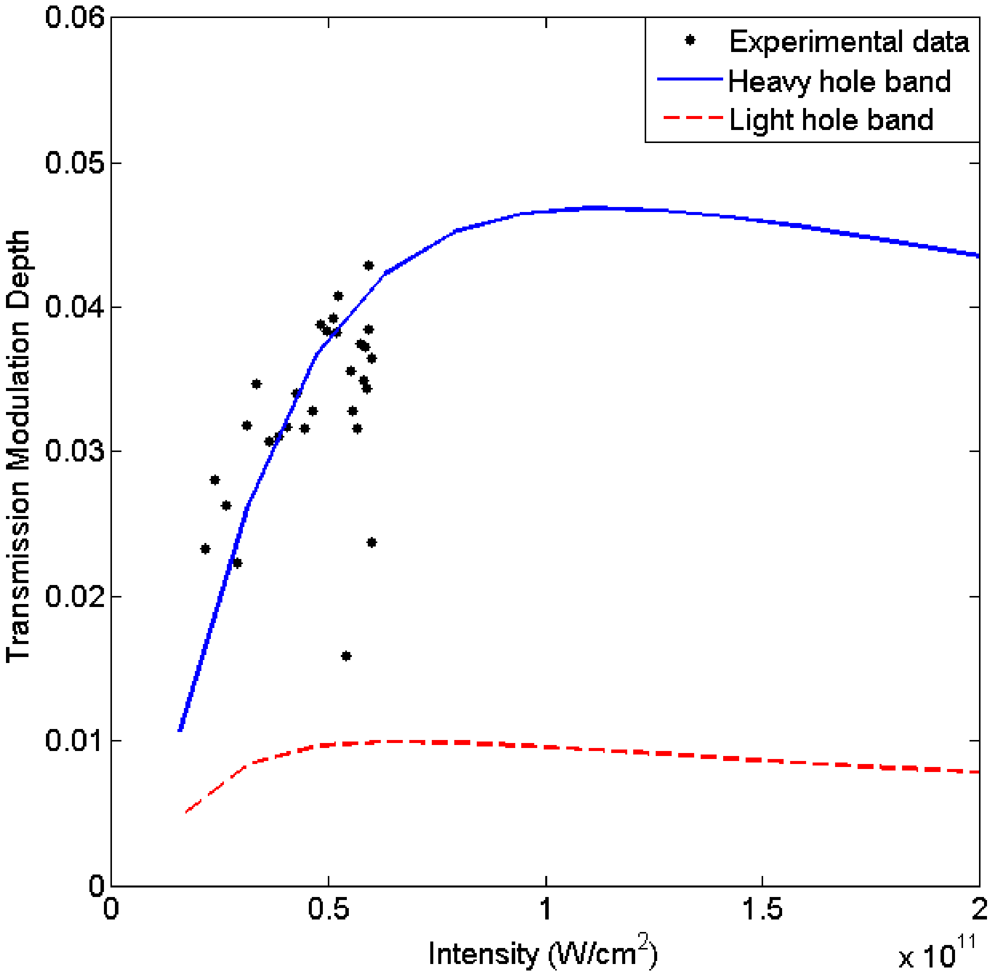

Figure 5.6: Modulation depth for transmission of 1900nm, 75fs pulse through a 600μm (100) GaAs, as a function of changing intensity. The points represent the experimental data and the solid blue and dashed red lines are the Keldysh transmission curves for the heavy and light hole band ionization respectively.

5.5 3100nm Transmission Modulation

In this section, we show the preliminary results for transmission of a 3100nm wavelength laser through a (100)GaAs crystal. The laser system responsible for creating this wavelength is described in section 4.3. The goal of this experimental set is to repeat the experiments done with 1900nm, with a longer wavelength, which pushes the ionization further into the tunnelling regime. This is of interest, since such experiments more closely resemble the ultrafast experiments done with single atoms and molecules. For this wavelength, we have a photon energy of 0.4eV and expect a 4-photon absorption to occur within the GaAs sample.

The 3100nm results shown here are preliminary in that we did not use the proper detector in their measurements. An InGaAs photodiode is used to capture the reference and transmission signals. However, the responsivity range of this detector is only known from 1.2μm to 2.6μm and the responsivity can not be found beyond this wavelength range. Although we did detect a sizable signal with the detectors, these sets of experiments will need to be redone with a new detector where the responsivity at 3100nm is established. Laser sources at these wavelengths have only recently become available[7]. Therefore there is very little instrumentation available for this wavelength range.

Nonetheless, we show the preliminary transmission and transmission modulation curves using 3100nm. The modulation curves indeed show the evidence of four-fold symmetry as expected for the cubic GaAs crystal.

The transmission of a 3100nm laser beam through (100)GaAs as a function of laser intensity is displayed in Fig.5.7. The laser is running at 100kHz, with a pulse duration of 92fs FWHM and is sent through a 10cm CaF_2 focusing lens. The transmission measurements are taken at a constant laser polarization angle of 0° with respect to the sample. In other words, the polarization is aligned along the [001] crystal axis. The points represent the experimental data, and the solid blue and dashed red curves represent the theoretical ionization curves for the heavy and light hole valence bands respectively. A similar intensity calibration method as used for the 1900nm is applied with the 3100nm results.

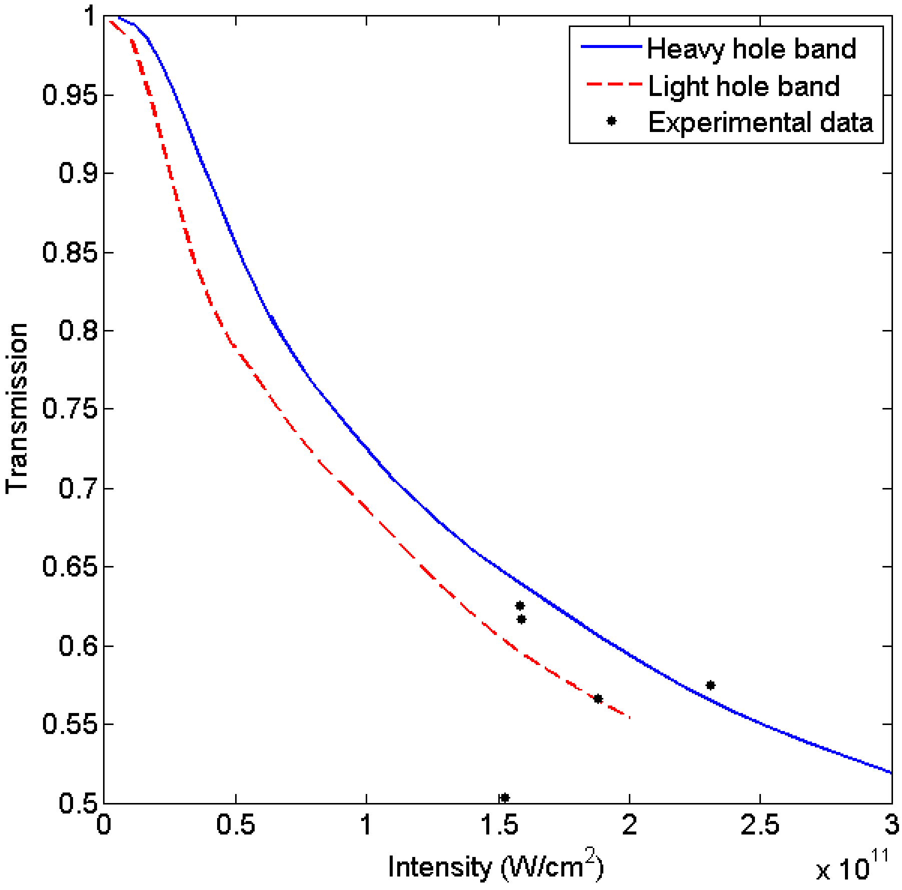

Figure 5.7: Transmission of a 3100nm laser pulse propagating through 600μm GaAs, aligned along (100) axis. Pulse duration is 92fs FWHM.The points represent the experimental data and the solid blue and dashed red lines are the intensity-averaged theoretical transmission curves for the heavy and light hole band ionization respectively.

The sample is rotated as a function of laser polarization and the transmission is gathered for each angle. The modulation that occurred for a transmission $\sim$ 0.57 is shown in Fig. 5.8. The blue curve shows the experimental data and the red line is the $\sin^2(2\theta)$ fitting. The fitting error is nearly 15% which is due to the pulse-to-pulse fluctuation of the laser. The modulation clearly shows the four-fold symmetry of the cubic GaAs crystal. Similar curves are found for all points shown in the transmission curve of Fig.5.7. The modulation depth in this curve is 26%. For all the data accumulated, the modulation depth ranged from 14% to 26%. As calculated theoretically (chapter 3), the heavy hole reduced effective mass ionization rate varies by 33% as a function of angle rotation. These modulation depths are significantly larger than what was seen in the previous work in dielectrics by Gertsvolf *et.al* [10], where modulation depth of 0.2% to 1% were observed, as well as in the 1900nm results discussed in this thesis, where the modulation depths ranged from 2% to 5%. As to why these modulation depths are so large may be attributed to the fact that the ionization of carriers within these experiments is further in the tunnelling regime than all other previous work. When carriers are ionized in the tunnelling regime, they have a more defined direction of propagation after ionization. Thus the carriers will follow more closely the strong variation in the effective mass as a function of angle. This behaviour has been shown in results from atomic ionization [5] where transverse uncertainty in the electron's momentum is small in the tunnelling regime. Therefore these preliminary results in modulation depth confirm that ionization in GaAs with 3100nm pulses is a better scaled representation of ultrafast atomic ionization. For this reason, we conclude that longer wavelengths are ideal for studying the structure of solid samples.

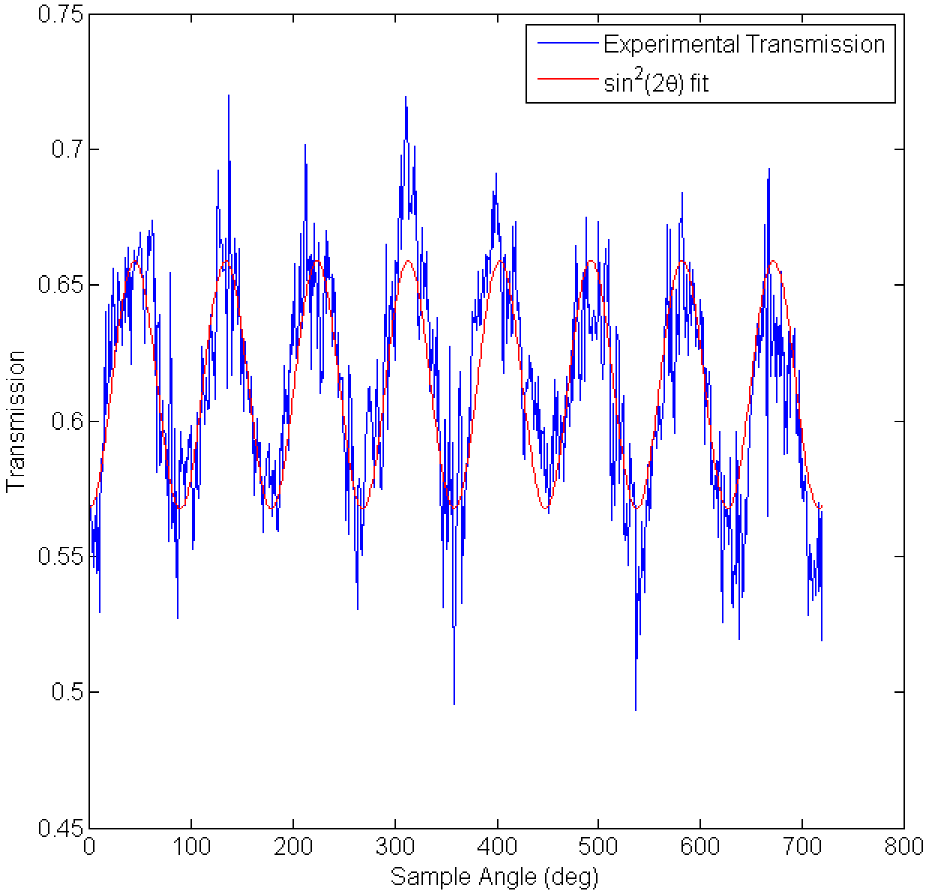

Figure 5.8: Modulation of transmission through 600μm (100)GaAs with a 92fs, 3100nm laser pulse.

The modulation depth as a function of laser intensity is plotted in Fig. 5.9. The points are the experimental data and the blue and red curves are the theoretical ionization curves for the heavy and light hole valence bands respectively. The overall behaviour of the theoretical curves can be explained follows using the same arguments as for the modulation depth results of 1900nm. The main difference between the 1900nm and 3100nm modulation curves can be seen in the presence of rich structure of the 3100nm theoretical curve. Such a difference can be explained by viewing the ionization rates of 1900nm and 3100nm shown in Fig. 3.3, where we see a structure in the 3100nm curve due to the presence of channel closing.

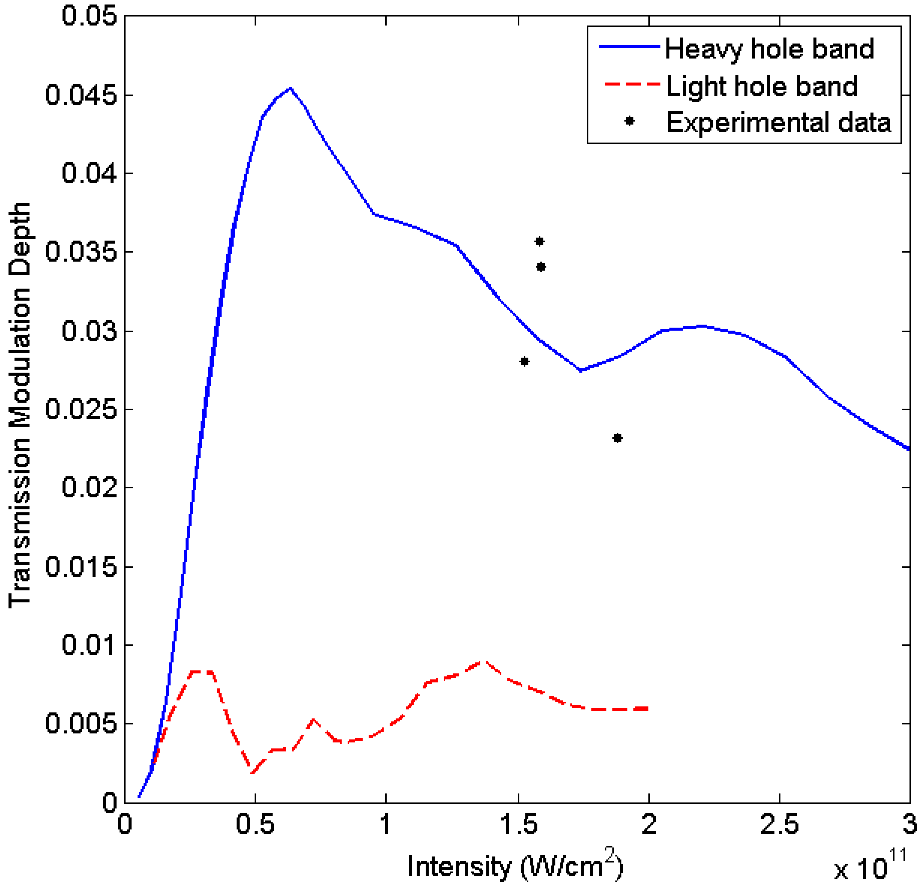

Figure 5.9: Modulation depth for transmission of 3100nm, 92fs, 100kHz pulse through 600μm (100)GaAs, as a function of intensity. The points represent the experimental data and the solid blue line and the dashed red line represent the theoretical modulation depth as predicted by Keldysh for the heavy hole band and light hole band ionization respectively.

In Fig. 5.10, we plot the peak ionization rate for a 3100nm beam, using a heavy-hole reduced effective mass. The smooth blue curve and red dashed curves represent the ionization rates corresponding to a sample angle of 0° and 45° respectively. The structure in the curves are explained by channel closing, as mentioned earlier in regards to Fig. 3.1. As the intensity increases, the effective bandgap of GaAs increases as seen in eqn.(3.5) which reads,

$$\tilde{\Delta} = E_g + \frac{e^2 F}{4m^* \omega^2} \tag{5.8}$$

where F, and ω are the electric field strength and laser frequency respectively.

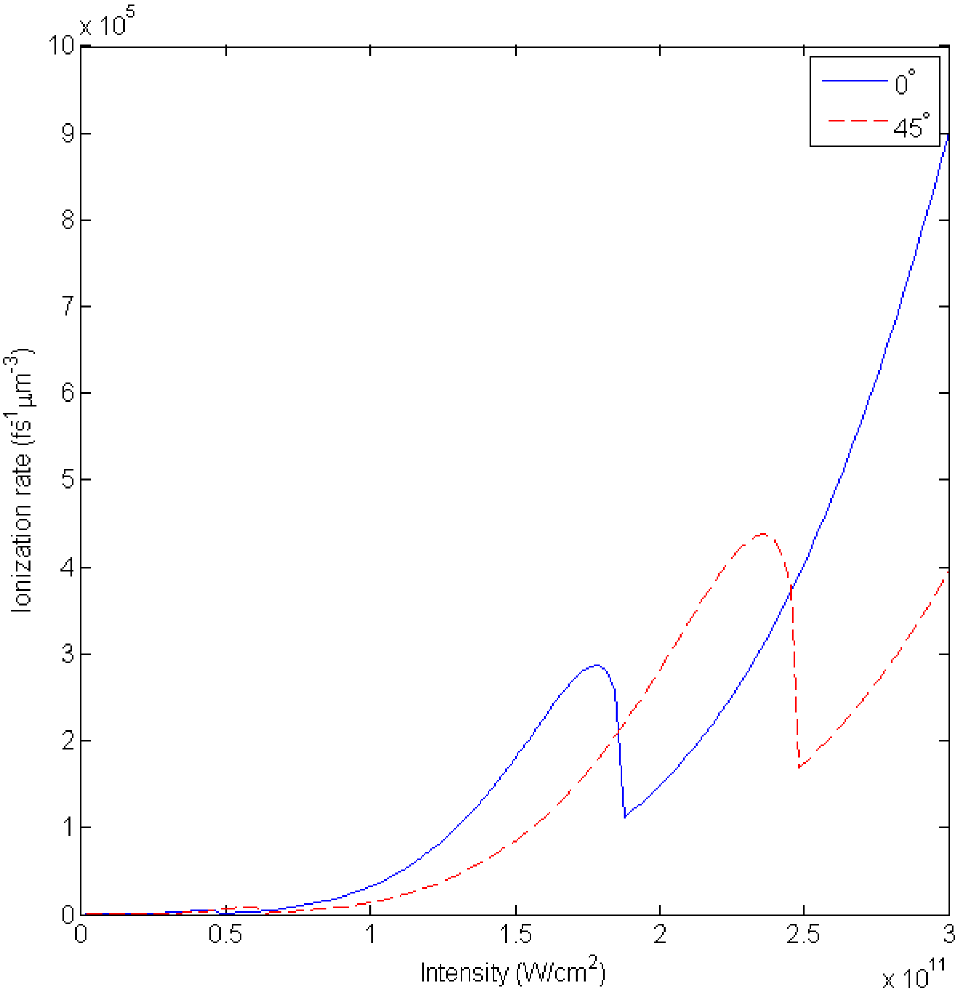

Figure 5.10: Peak Keldysh ionization rate for a 3100nm, 92fs FWHM pulse inside a GaAs sample. The smooth blue curve and red dashed curves represent the rate for a sample angle of 0° and 45° respectively. The reduced effective mass uses the heavy hole valence band.

In the perturbative multiphoton (MPI) regime, when the effective bandgap reaches the next multiphoton order, the ionization rate decreases sharply since the rate depends nonlinearly on the number of photons. This is clearly demonstrated by the local minima (dips) in Fig.5.10. This structure can also be explained via the ponderomotive potential energy, U_p, given by expression,

$$U_p = \frac{e^2 F}{4m^* \omega^2} \tag{5.9}$$

In the MPI ionization limit, the effective bandgap is equal to the bandgap plus the ponderomotive energy as seen above. Ponderomotive energy is the time-averaged kinetic energy of an electron in an electric field. Thus, the more intense the field, the more energy the electron needs to overcome the barrier and have sufficient ponderomotive energy in the conduction band. Yet another way of explaining the presence of the dips in the ionization rate is in terms of the AC Stark shift. For high lying states, the AC stark shift is equivalent to the ponderomotive potential energy [8, 9]. We can think of the Stark shift as being responsible for the channel closing. The shift of the minima in the ionization rate between the two curves in Fig. 5.10 can be explained as follows. The two curves correspond to different sample angles (0° and 45°), and thus have different effective masses. Since clearly the effective bandgap depends on the effective mass of solid, this explains the apparent shift in ionization rate dips between the two curves.

We now directly use Fig. 5.10 to explain the structure seen in the modulation depth in Fig. 5.9. The dips in the ionization rate structure of Fig. 5.10 occur at different intensities for each curve. As well, the curves increase at different slopes. Thus, the modulation depth which effectively measures the difference between the two ionization rates at a given intensity, will show a minima and maxima that follow the structure of the ionization rate for each effective mass. For example, the 0° blue curve and 45° red dashed curve cross at $\sim 1.7\text{x}10^{11}$ W/cm^2 which corresponds to a dip in the modulation depth at the same intensity, as seen in Fig. 5.9. Again, the ionization rate curves cross at an intensity of $\sim 2.4\text{x}10^{11}$ W/cm^2. The modulation depth in Fig. 5.9 begins a decline in the modulation depth.

In Fig. 5.9, it is evident that the experimental data is more closely predicted by the heavy hole band ionization than the light hole band ionization. This is identical to the results seen with the 1900nm experiments.

Chapter 6

Discussion and Outlook

We have shown experimentally that the multiphoton ionization (band-to-band excitation) rate of (100)GaAs follows the crystal's structure. This was seen by rotating a laser polarization with respect to the crystal axis, and viewing the laser transmission. With a 1900nm laser, we saw distinct modulation in the transmission in both hard and soft focusing experimental conditions. The laser transmission modulation repeated every 90°, which is congruous to the four-fold symmetry of a GaAs cubic FCC crystal. This followed similar results seen by Gertsvolf *et.al.* [10] with dielectrics, but with the added ability to predict the results using Keldysh ionization theory for solids [13]. Additionally, the modulation depth was much greater than seen in any previous work. Thus the changes in transmission could be seen in real-time without the need for Fourier transforms.

With a softly-focused setup (meaning that the laser focus Rayleigh range was greater than the sample thickness), the transmission as well as the modulation depth are well-predicted by Keldysh ionization theory. In this theory, ionization depends on the reduced effective mass, which results from the curvature of the bandstructure along different directions of laser polarization. We showed that the modulated transmission results primarily from ionization between the heavy-hole valence band and first conduction band. This is clearly seen in Fig.5.6 where the experimental data clearly follows the curve as predicted using Keldysh ionization from the GaAs heavy hole valence band, using the reduced effective mass. Although the ionization rate of the light hole valence band is greater than for the heavy holes, as seen in Fig.3.2, the heavy hole valence band shows a much greater variation in effective mass as a function of angle. As an example, the ionization rate from the heavy hole band varies by 33.7% while the light hole band varies by only 8.7% for a peak intensity of 10×10^{10} W/cm^2. Next, the phase of the ionization rate for the heavy and light hole bands differs by 90°, as seen in Fig.2.7. The phase of the heavy hole ionization corresponds exactly to what was seen in experiment (see Fig.5.5). In addition, the density of states for the heavy hole valence band is much greater than for the light hole valence band, as seen in Fig.2.5. This means that there are significantly more heavy hole carriers available for ionization than from the light hole band. So although ionization occurred from both bands, the modulation in transmission is due primarily to the variation in the heavy hole effective mass.

In order to push the experiments further into the tunnelling regime, we performed preliminary experiments with a 3100nm laser. We saw four-fold modulation in the laser transmission, as was seen with the 1900nm laser. However, these experiments require additional alterations in order to be accurately predicted with an ionization model. First, a new way of attenuating the laser energy needs to be implemented. Currently, the beam is attenuated by delaying the temporal overlap of the seed and pump in the final amplifying OPA pass of the laser system. This however, makes the range of possible pulse energies very small and may introduce variations in the pulse spectrum. Second, the pulse-to-pulse fluctuation of the laser reached in excess of 15%, which increased the error in the measurements. Third, the InGaAs photodiode detectors used, only have a known responsivity up to 2600nm. The spectrum of the OPCPA laser has a centre at 3100nm, and the bandwidth extends from 2900nm to 3300nm. The trend of the photodiode responsivity decreases from the maximum located at ~2200nm. So at 3100nm, the likely responsivity is extremely small and it may even be possible that the signal being detected is residual second-harmonic signal in the laser beam, arising from the OPCPA laser system. It is of uttermost importance that new detectors be recruited to complete these sets of experiments.

Through the results in this thesis, we have produced influential headway for both fundamental and application science. Fundamentally, we have created a link between condensed matter physics and the more popular research done in atomic and molecular optical (AMO) sciences. The experiments performed in this thesis are analogous to the mapping of molecular orbitals using ionization yield [20]. In both types of experiments, the ionization rate depends directly on the shape of the electron distribution. Strong evidence of this fact is observed when changing the laser polarization with respect to the crystal/molecular axis. Until recently, tunnelling ionization in atoms and molecules was thought to be possible only from the electron highest occupied molecular orbital (HOMO), due to the highly nonlinear behaviour of ionization. Such a hypothesis has now been disproved in [18, 23]. In these results, the authors showed that ionization can occur from HOMO or HOMO^{-1}, because the ionization rate depends on the angular distribution of the electron density and the angular shape is different for the two orbitals. In GaAs, the HOMO and HOMO^{-1} in molecules are analogous to the light and heavy hole valence bands. Therefore in the future we may also be able to differentiate between the light and heavy hole ionization rates.

Recently, Ghimire *et.al.* [11] have shown the first experimental evidence of high harmonic generation (HHG) produced in a bulk semiconductor. Creation of HHG in solids is a current topic of research in that it can lead to production of bright, short wavelength radiation of high intensities. The authors in [11] showed harmonics up to the 25th order in a ZnO crystal using 3.25μm laser radiation, in the tunnelling regime. The laser was sent normally to the crystal c axis and the laser transmission was sent through a grating, where the harmonics could be detected. The high harmonics were said to correspond to modulations in the Bloch oscillations within the crystal lattice. This was attributed to a combination of electron Bragg scattering off the Brillouin zone near the peaks of the electric field and the anharmonic electron motion within the conduction band. Most interestingly, they showed a dependence on the HHG intensity with the angle between the crystal axis and the laser polarization. Our studies are relevant to high harmonic generation (HHG) in solid samples, because we have studied the effect of crystal structure on ionization, which is the first step in the high harmonic generation process. We have highlighted several important properties of ionization. First, we looked at how ionization occurs inside a solid and how it varies with crystal orientation. These results may account for the variation of HHG intensity with crystal angle. Second, we then looked at the relative contribution from light and heavy hole valence bands. For each band, the carrier effective mass is different, so the corresponding Bloch oscillations would also be different. Third, we showed that the effective bandgap plays a role in ionization. It would be interesting to see if HHG intensity could show evidence of channel closing.

Through our results, we open up opportunities for technology in non-invasive and real-time crystallography. The intensities used are far below the damage threshold for GaAs and the laser transmission showed no change even after multiple sample rotations. Thus crystallography can be performed while leaving the samples intact. More common crystallographic techniques such as Bragg/X-ray diffraction require destruction of the sample, thus giving this new crystallography technique an immediate advantage. In this thesis we focused on softly focused laser beams, but we have also showed that similar qualitative conclusions can be obtained from hard-focusing laser setups. So we have already shown that it is possible to see the structure at highly localized points within a bulk material. At the limit, we may reach wavelength resolutions or better, due to the highly nonlinear behaviour of ionization. Due to the real-time characteristic of this technology, it may be possible to view phase changes such as melting and/or freezing in real-time. This may open up new methods of experimentation in physical chemistry.

For example, GaN is becoming a popular semiconductor of interest for use in LED and blue-diode research. Crystallography techniques may be useful in improving crystal quality control, by looking at defects in crystal structure. Even small defects may create short circuits or other problems. The technology may allow for detection of crystal boundaries and is well suited for 3D applications.

This technology may also be applied to more complicated media, such as biological tissues. Many tissues, such as muscles have directionality, which may be probed using crystallographic techniques to determine the orientation of some of the smallest cellular components. Now, the non-invasive nature of this application may be called into check since tissues tend to have a much smaller damage threshold. However, this may be useful in ex-vivo samples. This creates a new and different kind of multiphoton microscopy.

Bibliography

[1] ABINIT, http://www.abinit.org/.

[2] CVI Melles-Griot catalogue, April 2011.

[3] Sadao Adachi. *Bulk GaAs and Related Materials.* World Scientific, 1994.

[4] M. V. Ammosov, N. B. Delone, and V. P. Krainov. Tunnel ionization of complex atoms and of atomic ions in an alternating electromagnetic field. *Sov Phys JETP*, 64(6):1191, 1986.

[5] L. Arissian, C. Smeenk, F. Turner, C. Trallero, A. V. Sokolov, D. M. Villeneuve, A. Staudte, and P. B. Corkum. Direct test of laser tunneling with electron momentum imaging. *Phys. Rev. Lett.*, 105:133002, 2010.

[6] Robert W. Boyd. *Nonlinear Optics.* Academic Press, 2008.

[7] O. Chalus, P. K. Bates, M. Smolarski, and J. Biegert. Mid-IR short-pulse OPCPA with micro-joule energy at 100kHz. *Opt. Express*, 17(5):3587–3594.

[8] S. L. Chin, Claude Rolland, P. B. Corkum, and Paul Kelly. Multiphoton ionization of xe and kr with intense 0.62-μm femtosecond pulses. *Phys. Rev. Lett.*, 61:153–156, Jul 1988.

[9] R. R. Freeman, P. H. Bucksbaum, H. Milchberg, S. Darack, D. Schumacher, and M. E. Geusic. Above-threshold ionization with subpicosecond laser pulses. *Phys. Rev. Lett.*, 59:1092–1095, Sep 1987.

[10] M. Gertsvolf, H. Jean-Ruel, P. P. Rajeev, D. D. Klug, D. M. Rayner, and P. B. Corkum. Orientation-dependent multiphoton ionization in wide band gap crystals. 101:243001, 2008.

[11] Shambhu Ghimire, Anthony D. DiChiara, Emily Sistrunk, Pierre Agostini, Louis F. DiMauro, and David A. Reis. Observation of high-order harmonic generation in a bulk crystal. *Nature Phys.*, 7:138–141, May 2010.

[12] L. V. Keldysh. Behavior of non-metallic crystals in strong electric fields. *Sov. Phys. JETP*, 6 (33)(4):763, 1958.

[13] L. V. Keldysh. Ionization in field of a strong electromagnetic wave. *Sov Phys JETP*, 20(5):1307, 1965.

[14] Charles Kittel. *Introduction to Solid State Physics.* John Wiley and Sons, Hoboken, N. J., 1996.

[15] M. Levinshtein. *Handbook on Semiconductor Parameters.* World Scientific, 1996.

[16] I. V. Litvinyuk, K. F. Lee, P. W. Dooley, D. M. Rayner, D. M. Villeneuve, and P. B. Corkum. Alignment-dependent strong field ionization of molecules. *Phys. Rev. Lett.*, 90(23):233003.

[17] Michael P. Marder. *Condensed Matter Physics.* John Wiley and Sons, New York, N.Y., 2000.

[18] Brian K. McFarland, Joseph P. Farrell, Philip H. Bucksbaum, and Markus G*ü*hr. High harmonic generation from multiple orbitals in N_2. *Science*, 322(5905):1232–1235, 2008.

[19] P.W. Milonni and J.H. Eberly. *Lasers.* Wiley Series in Pure and Applied Optics. Wiley, 1988.

[20] D. Pavičić, K. F. Lee, D. M. Rayner, P. B. Corkum, and D. M. Villeneuve. Direct measurement of the angular dependence of ionization for N_2, O_2, and CO_2 in intense laser fields. *Phys. Rev. Lett.*, 98(24):243001, 2007.

[21] A. M. Perelomov, V. S. Popov, and M. V. Terent'ev. Ionization of atoms in an alternating electric field. *Sov. Phys. JETP*, 23(5), 1966.

[22] A. Savitzky and M. J. E. Golay. Smoothing and differentiation of data by simplified least squares procedures. *Anal. Chem.*, 36(8):1627–1639, 1964.

[23] Olga Smirnova, Yann Mairesse, Serguei Patchkovskii, Nirit Dudovich, David Villeneuve, Paul Corkum, and Misha Yu. Ivanov. High harmonic interferometry of multi-electron dynamics in molecules. *Nature*, 460:972–977, August 2009.

[24] X. M. Tong, Z. X. Zhao, and C. D. Lin. Theory of molecular tunneling ionization. *Phys. Rev. A*, 66:033402, 2002.

[25] S. M. Woodley and R. Catlow. Crystal structure prediction from first principles. *Nature Materials*, 2008.

Appendix A

GaAs Sellmeier Coefficients

The Sellmeier coefficients (λ in microns, T = 297 K) are given below for GaAs [2]. From these coefficients, we find several parameters for changing wavelengths as stated above in table (2.1), which are used in the calculations.

$$\begin{aligned}
n_0^2 &= 1 + \frac{B_1\lambda^2}{\lambda^2 - C_1} + \frac{B_2\lambda^2}{\lambda^2 - C_2} + \frac{B_3\lambda^2}{\lambda^2 - C_3} \\
B_1 &= 2.5 \\
B_2 &= 7.4969 \\
B_3 &= 1.9347 \\
C_1 &= 0 \\
C_2 &= 16.663 \times 10^{-2} \\
C_3 &= 1382
\end{aligned} \tag{A.1}$$

Appendix B

Reciprocal Space Conversion

The density functional theory (DFT) bandstructure calculation was performed for equally spaced divisions (in reciprocal space) about the propagation axis. Due to the four-fold symmetry of the crystal in both real-space and reciprocal space, it is only necessary to derive the angles for the first quadrant (90°) of the crystal. Within this quadrant, we only need to look at the rotation of the electric field from points X to W and W to W', since the last portion is the reflection of the X to W rotation.

When referring to directions in real space, we refer to the primitive lattice directions, which for a face-centred cubic (FCC) lattice is given by,

$$\begin{aligned} \vec{a_1} &= \frac{a}{2}(\hat{x}+\hat{y}) \\ \vec{a_2} &= \frac{a}{2}(\hat{y}+\hat{z}) \\ \vec{a_3} &= \frac{a}{2}(\hat{z}+\hat{x}) \end{aligned} \tag{B.1}$$

where a is the length of the unit cell and $\hat{x}, \hat{y}, \hat{z}$ are the unit vectors along the Cartesian coordinates.

For reference, we refer to the GaAs reciprocal lattice (first Brillouin zone) as shown in Fig. 2.3. The first Brillouin zone has a cubic symmetry as in the real-space lattice, when propagation along one of the reciprocal major lattices.

In order to transform from real-space to reciprocal space, we use the conversion formula [14],

$$\vec{b_i} = \frac{2\pi}{a} \frac{\vec{a_j} \times \vec{a_k}}{\vec{a_i} \cdot \vec{a_j} \times \vec{a_k}} \tag{B.2}$$

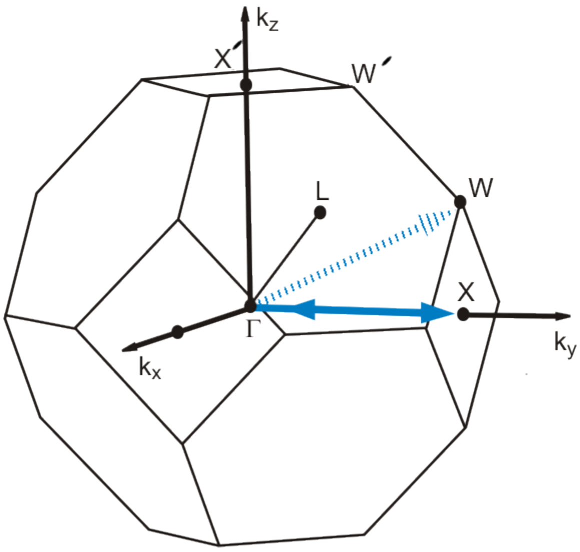

Figure B.1: GaAs reciprocal lattice (first Brillouin zone) . The propagation axes are marked as k_i. The high symmetry points are labelled Γ, X, K, L.

where b_i are the primitive reciprocal lattice vectors, which when converted into Cartesian coordinates, gives [14],

$$\begin{aligned} \vec{b}_1 &= \frac{2\pi}{a}(-\hat{x}+\hat{y}+\hat{z}) \\ \vec{b}_2 &= \frac{2\pi}{a}(\hat{x}-\hat{y}+\hat{z}) \\ \vec{b}_3 &= \frac{2\pi}{a}(\hat{x}+\hat{y}-\hat{z}) \end{aligned} \tag{B.3}$$

Due to symmetry flexibility, we choose to align the Γ to X axis (labelled the X vector) along the [010] axis, in other words, the $+\hat{y}$-axis. (Note that this notation means that the [010] axis runs perpendicular to the (010) plane which exists in the $\vec{a_1} - \vec{a_3}$ plane). The [010] axis by definition, is the same as the a_2 axis. When we convert this into reciprocal space using eqn.(B.2), we get

$$X = \frac{2\pi}{a}\hat{y}$$

Thus the X vector can also be written as $X = \frac{1}{2}(\vec{b}_1 + \vec{b}_3)$ or $(\frac{1}{2}\ 0\ \frac{1}{2})$ in reciprocal space. The Z$_n$ symmetry points between X and W are incremental positions as the electric field polarization is rotated from the X symmetry point to the W symmetry point. The FCC Brillouin zone is the same as the body-centred cubic (BCC) Wigner-

Seitz cell. By using this knowledge, the W point in reciprocal space for rotation about [100] is ($\frac{3}{4}$ $\frac{1}{4}$ $\frac{1}{2}$) in reciprocal space. To rotate from X to W, we increment the $\vec{g}_2$ and $\vec{g}_3$ vectors by a total of $\frac{1}{4}$ to reach W. Mathematically,

$$\begin{aligned} Z_n &= \left(\frac{1}{2} + n\alpha\right)\vec{g}_1 + n\alpha\vec{g}_2 + \frac{1}{2}\vec{g}_3 && \text{(B.4)} \\ &= \frac{2\pi}{a}\hat{y} + \frac{4\pi n\alpha}{a}\hat{z} && \text{(B.5)} \end{aligned}$$

where n is an integer step and α is the incremental value that when multiplied by the total number of steps gives $\frac{1}{4}$.

Next, we look at the rotation of the electric field from point W to W', labelled as K$_n$. The W symmetry point is ($\frac{3}{4}$ $\frac{1}{4}$ $\frac{1}{2}$) and W$'$ is ($\frac{3}{4}$ $\frac{1}{2}$ $\frac{1}{4}$). Mathematically, this makes K$_n$,

$$\begin{aligned} K_n &= \frac{3}{4}\vec{g}_1 + \left(\frac{1}{4} + n\alpha\right)\vec{g}_2 + \left(\frac{1}{2} - n\alpha\right)\vec{g}_3 \\ &= \frac{2\pi}{a}\hat{y} + \frac{\pi}{a}\hat{z} + \frac{4\pi n\alpha}{a}(\hat{z} - \hat{y}) && \text{(B.6)} \end{aligned}$$

Appendix C

Threshold Ionization, Intensity Relationship

We use a classical over-the-barrier single-atom ionization model to find the relationship between the atomic ionization potential and minimum laser intensity necessary to singly ionize an atom.

In Fig.C.1, we show the general form of an atomic potential energy well, represented with the black curve. The vertical direction represents potential energy; zero being the top of the black curve. The horizontal direction is distance, represented by the variable, r, and is measured from the centre of the energy well. The blue curve is the identical atomic potential energy undergoing a deformation due to a laser electric field. We highlight with the dotted line, the peak value of the deformed blue curve. We define the intensity threshold as the minimum intensity required to deform the potential energy curve to a level below the ionization potential, I_p. At this point, the electron can escape the atomic potential well.

We now solve for the threshold intensity, at which this process occurs. The expression for the deformed potential energy is given by

$$U(r) = \frac{Qe}{4\pi\varepsilon_0 r} + eEr \tag{C.1}$$

where Q is the atomic charge, and E is the laser electric field. The electric field is approximated to be constant in space. At the peak of the deformed potential energy curve, the following conditions apply:

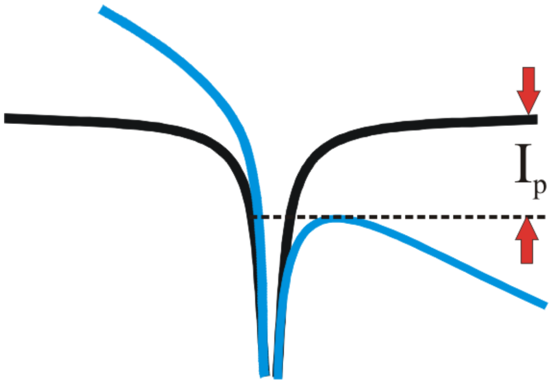

Figure C.1: An atomic potential energy well (shown in the black curve) experiences a deformation (shown by blue curve) due to a laser electric field. The dotted line denotes the peak value of the deformed blue curve. The laser intensity is such that the potential energy difference between the deformed and non-deformed curves is equal to the ionization potential.

$$\begin{aligned} \frac{\partial U(r_{pk})}{\partial r} &= 0 \\ U(r_{pk}) &= I_p \end{aligned}$$

The subscript, pk, denotes the radial distance at which the potential curve maximum occurs. We apply the first above condition to eqn. (C.1). First, we solve for r_{pk} which equals

$$r_{pk} = \left(\frac{Q}{4\pi\varepsilon_0 E_{th}}\right)^{1/2} \tag{C.2}$$

E_{th} is the threshold electric field. By substituting this back into eqn.(C.1), and applying the remaining condition, the laser electric field is written as

$$E_{th} = \left(\frac{\pi\varepsilon_0}{Qe^2}\right) I_p^2 \tag{C.3}$$

Since intensity depends on the square of the electric field, the threshold ionization is proportional to the fourth power of the ionization potential.

Appendix D

Spatial Mode Characterization

We describe the steps involved in performing a laser spot-size measurement using the knife-edge method. This measurement was performed at two positions after the OPA output to determine the beam radius before the focusing lens and note any divergence that may be present in the beam.

Two positions are chosen for the measurements; one directly after the shutter and the other directly before the focusing lens. Refer to Fig.4.4 for a visual schematic of the placement locations. The distance from the two points is 132cm. A razor blade is mounted onto a translation stage which can slide in and out of the beam. A gauge measures the relative position of the blade in increments of 0.01mm. The knife-edge measurement is performed both in the x and y directions. An InGaAs photodiode is used to measure the laser signal after the blade.

We show in Fig.D the experimental data of the knife-edge measurements. The four figures represent the x and y measurement for two different positions. The azimuthal axis shows the relative position of the razor blade in mm. The ordinate axis gives the photodiode measurements in mV for the respective blade position. We assume a Gaussian mode and thus the curves are fit to an error function as shown in the red curves. The error function used for fitting is,

$$erf(x) = A\frac{2}{\sqrt{\pi}}\int_0^{\alpha} exp(-t^2)dt \tag{D.1}$$

where A is a constant, and $\alpha = \sqrt{2}(x - \mu)/w$ where μ is the mean (arbitrary) position of the error function and w is the beam waist (1/e in field). The $\sqrt{2}$ is used to convert the beam radius from the measured 1/e radius value in intensity, as given from the photodiode signal, to the 1/e value of the radius in the field. By viewing

Table D.1: Knife-Edge Beam Radii

	x	y
Position 1, w (mm)	1.01	1.22
Position 2, w (mm)	1.08	1.21
Divergence (mrad)	0.0547	-0.00457

Fig.D, we see that the laser modes are not perfectly Gaussian. First, the curves do no fit perfectly to an error function. Second, the beam radii as measured for the x and y directions are not identical. However, we estimate the beam's x and y radii from the curve fitting functions. The divergence is found by taking the difference in the beam radii for the two positions over the distance between the positions. We summarize the findings in Table D.1. We use the radius from position 2 as the beam radius entering the focusing lens. The beam spot is elliptical with the x dimension larger than the y dimension.

The beam mode is not circular, but has an elliptical mode. For intensity calculation purposes, we will take the area of the elliptical mode (A $= \pi w_x w_y$) and find the corresponding circular radius for the equivalent area, assuming a circular mode. Position 2 will be used for finding the mode radius. From this we get a circular radius of 1.1mm. The peak intensity of the laser pulse can be estimated using the method derived in Appendix E.

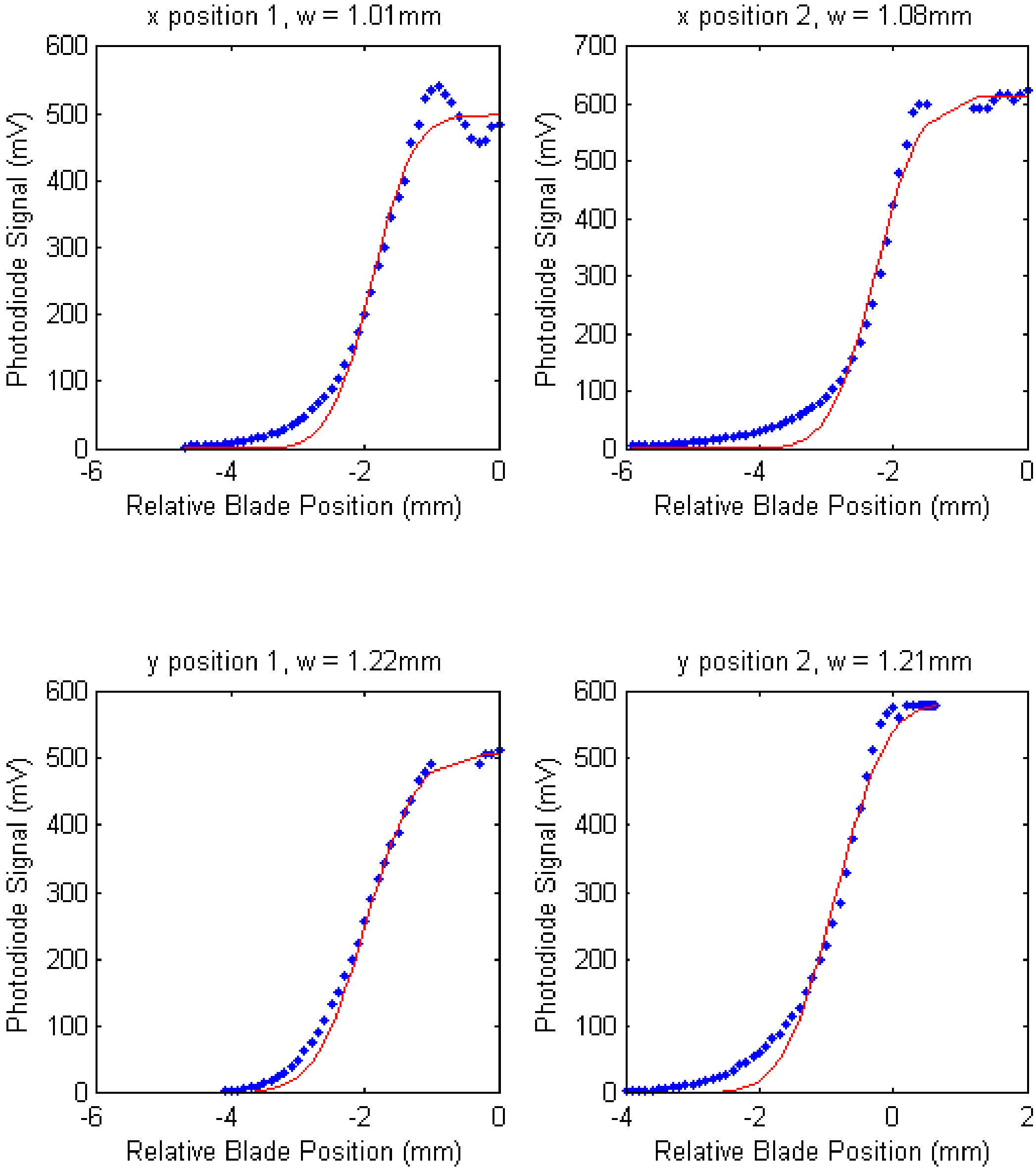

Figure D.1: Photodiode signal of a knife-edge measurement for the OPA laser system. Two positions in both the x and y coordinates are shown. The title gives the respective position and coordinate in addition to the beam radius corresponding to that measurement. The red lines represent the fit of an error function from which the beam radius is retrieved.

Appendix E

Intensity Derivations

In this appendix, we calculate the relationship between the pulse energy and peak intensity. First we assume a Gaussian pulse profile in both the temporal, t, and radial, r, coordinates, and derive the relationship. From this expression, we will estimate the experimental focusing conditions to achieve necessary peak intensities. The exact peak intensity will then be determined by fitting the experimental transmission-energy curves to the transmission-intensity curves created by space-time averaged Keldysh theory (See chapter 3).

Starting from the Gaussian electric field, the intensity can be written as a separation of variables in space and time [6],

$$\begin{aligned} I(r,z,t) &= I(r,z)I(t) \\ I(r,z) &= I_0 \left(\frac{w_0}{w(z)}\right)^2 exp\left(-\frac{2r^2}{w^2(z)}\right) \\ I(t) &= exp\left(-\frac{t^2}{\tau^2}\right) cos(\omega t) \end{aligned}$$

where z is the propagation axis, $w(z)$ is the spatially-dependent beam radius, and w_0 is the minimum beam radius, 1/e in field. I_0 is the peak intensity and τ is the 1/e pulse duration in intensity. To find the peak energy relationship, we choose a stationary point in the propagation ($z = 0$), where $w(z = 0) = w_0$.

To find the energy, the intensity must be integrated over both space and time. By integrating first over space, we find the power in the pulse, P_{pulse}.

$$
\begin{aligned}
P_{pulse} &= \int I(r,0)dA \\
&= \int_0^{\infty} I_0 exp\left(-\frac{2r^2}{w_0^2}\right) 2\pi r dr
\end{aligned}
$$

The integral is solved analytically by using the even symmetry of the integral, and implementing substitution. This gives the relationship,

$$P_{pulse} = \frac{1}{2} I_0 \pi w_0^2 \tag{E.1}$$

The total energy is then,

$$
\begin{aligned}
E &= \int_{-\infty}^{\infty} P_{pulse} I(t) dt \\
E &= \frac{1}{2}\pi\sqrt{\pi} I_0 w_0^2 \tau \qquad \text{(E.2)}
\end{aligned}
$$

For the 1900nm transmission in GaAs, we use a 75fs (FWHM) pulse with an input spot size of $w = 1.1$mm. We find the intensity inside the sample is 7 times less than what is predicted through Gaussian focusing. We have confidence in the actual intensity inside the sample because we have two experimental measurements that match our theoretical simulations, when using this intensity. The fact that the actual intensity in the sample is lower than the predicted Gaussian value is due to several reasons. First, we know that the beam profile is not Gaussian, as seen through the knife-edge measurements shown in Appendix D. Second, when calculating the Gaussian intensity, we assume a fixed pulse duration. However, the pulse profile is changing due to absorption. The absorption may be viewed as a "lawnmower" chopping off the pulse above the threshold intensity. This appears as an increased pulse duration which will decrease the effective intensity. Finally, slight adjustments were made regularly to the OPA in order to optimize output power and beam profile. Knife-edge measurements were not made on a daily basis and therefore the measurement quoted may not be identical to the experimental conditions.

For the 3100nm transmission in GaAs, we use a 92fs FWHM laser pulse. The input spot size is measured with a NanoScan system to be $\sim 150\mu$m. By fitting the experimental data to the GaAs ionization threshold, we determine the intensity inside the sample is 40 times less than is predicted by Gaussian focusing in eqn. (4.2). However, it was known during the experiments that the beam profile was not Gaussian. In addition, it is difficult to determine the beam spot using the technology available.

Appendix F

Hard Focusing Transmission

We find the experimental transmission of a 1900nm, 75fs (FWHM), 500Hz laser sent through (100)GaAs for the hard focusing condition. The setup as shown in Fig. 4.4 is used. An initial beam size of 1.1 mm is sent through a 35mm focusing lens. The transmission as a function of pulse energy is plotted in Fig. F.1. The pulse energy is found through a reference photodiode measurement and corresponding power calibration as described in chapter 4. The procedure and analysis techniques for the hard and soft focusing experiments is identical.

The transmission curve shows the presence of nonlinear ionization at low energy. The transmission begins to increase at energies around 4-5 μJ. As described in section 4.1, the hard focusing configuration may experience adverse phase advance effects. The large carrier excitation at higher intensities cause the refractive index to decrease at the peak of the pulse. The laser beam then diverges, causing the peak intensity to decrease. This decreases the amount of ionization which is revealed by an increase in laser transmission.

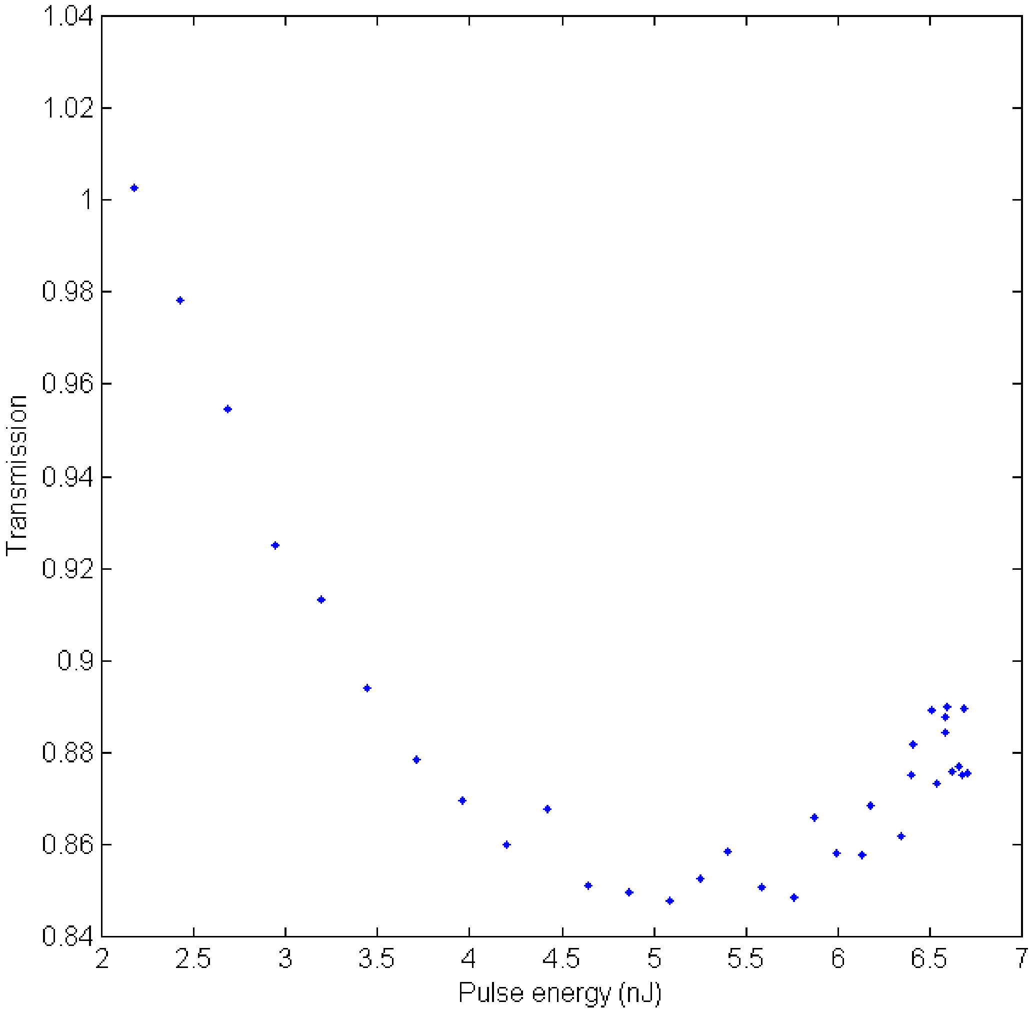

Figure F.1: Laser transmission through a 600μm sample of (100)GaAs for a tightly focused 75fs, 1900nm laser beam.